

# **Non-invasive monitoring of single-cell mechanics by acoustic scattering**

Joon Ho Kang<sup>1,2</sup>, Teemu P. Miettinen<sup>1,3</sup>, Lynna Chen<sup>4</sup>, Selim Olcum<sup>1</sup>, Georgios Katsikis<sup>1</sup>,  
Patrick S. Doyle<sup>1,5</sup>, Scott R. Manalis<sup>1,4,6\*</sup>

<sup>1</sup>Koch Institute for Integrative Cancer Research, Massachusetts Institute of Technology, Cambridge, MA, USA.

<sup>2</sup>Department of Physics, Massachusetts Institute of Technology, Cambridge, MA, USA.

<sup>3</sup>MRC Laboratory for Molecular Cell Biology, University College London, London, UK.

<sup>4</sup>Department of Biological Engineering, Massachusetts Institute of Technology, Cambridge, MA, USA.

<sup>5</sup>Department of Chemical Engineering, Massachusetts Institute of Technology, Cambridge, MA, USA.

<sup>6</sup>Department of Mechanical Engineering, Massachusetts Institute of Technology, Cambridge, MA, USA.

\*Corresponding author, email: [srm@mit.edu](mailto:srm@mit.edu)

## Abstract

Monitoring mechanics of the same cell throughout the cell cycle has been hampered by the invasiveness of mechanical measurements. Here, we quantify mechanical properties via acoustic scattering of waves from a cell inside a fluid-filled vibrating cantilever with a temporal resolution of <1 min. Through simulations, experiments with hydrogels and chemically perturbed cells, we show that our readout, the size-normalized acoustic scattering (SNACS), measures stiffness. We demonstrate the noninvasiveness of SNACS over successive cell cycles using measurements that result in < 15 nm deformations. Cells maintain constant SNACS throughout interphase but exhibit dynamic changes during mitosis. Our work provides a basis for understanding how growing cells maintain mechanical integrity and demonstrates that acoustic scattering can non-invasively probe subtle and transient dynamics.

## Introduction

Although spatiotemporal changes in cytoskeletal components have been widely characterized by optical microscopy<sup>1,2</sup>, mechanical measurements are necessary for fully understanding the functional consequences of cytoskeletal remodeling<sup>3</sup>. Mechanical properties of living cells such as stiffness often play a fundamental role in various intra- and intercellular processes such as migration<sup>4</sup>, metastasis<sup>5,6</sup> and development<sup>7</sup>. From atomic force microscopy (AFM)<sup>8,9</sup>, to optical stretching<sup>10-12</sup>, fluid shear stress<sup>13,14</sup> and particle tracking methods<sup>15-17</sup> numerous strategies have been introduced for measuring mechanical properties of single cells, yet they are typically invasive and used as end-point assays. Microindentation and AFM techniques are capable of continuous monitoring by probing stiffness changes through a series of indentations across the top surface of a cell<sup>18,19</sup>. However, these measurements are influenced by the location and geometry where the tip physically makes contact, which makes long-term monitoring of whole-cell stiffness with high temporal resolution challenging. Recently, acoustic fields have been used to non-invasively probe cellular stiffness<sup>20-22</sup>. This is typically achieved by applying acoustic radiation forces in microchannels and tracking the stiffness-dependent trajectories of cells in order to obtain end-point measurements.

Here we introduce an acoustic method for continuously and non-invasively monitoring single-cell mechanics over multiple cell generations. This enables us to precisely follow the mechanical dynamics of single cells in the time scales less than a minute and observe mechanical changes that are too subtle to be observed at the population level due to cellular heterogeneity.

## Results

### Acoustic scattering shifts resonant frequency at the node of a suspended microchannel resonator

We utilized the vibration of a suspended microchannel resonator (SMR, Fig. 1a, top) as an acoustic energy source and investigated if the scattered acoustic fields from the cell could provide a signal to monitor its mechanical properties (Fig. 1b). The SMR is a cantilever-based microfluidic mass sensor that has previously been used to measure cell buoyant mass<sup>23</sup>. Vibrating the SMR at its second mode (resonant frequency  $f$ ) causes the vibration amplitude to vary along the length of the cantilever, with one local maximum (antinode) near the center and a zero-minimum (node) near the tip (Fig. 1a, middle). When a cell is at the antinode, the net change in mass (i.e. the buoyant mass of the cell) corresponds to a change in the kinetic energy of the system<sup>24</sup>, and thus causes a shift in the resonant frequency of the SMR ( $\Delta f/f|_{\text{antinode}}$ ) (Fig. 1a, bottom and Supplementary Note 1). When the cell is at the node, the net change in mass is not expected to shift the resonant frequency ( $\Delta f/f|_{\text{node}} = 0$ ) because the vibration amplitude is zero and there is no change in kinetic energy. Surprisingly, we observed a consistent resonant frequency shift at the node ( $\Delta f/f|_{\text{node}} \neq 0$ ) when we flowed a single cell or polystyrene bead in the SMR (Fig 1a, bottom). This resonant frequency shift, which we termed “node deviation” ( $\Delta f/f|_{\text{node}}$ ), was different for cells and beads of similar buoyant mass. We therefore hypothesized that the node deviation corresponds to an energy change due to acoustic scattering from the cell’s surface, and that the node deviation depends on cellular mechanical properties.

First, to determine if the node deviation corresponds to acoustic scattering, we utilized Finite Element Method (FEM) simulations for fluid-structure acoustic interactions (Supplementary Note 2). This revealed that the acoustic pressures and velocities vary along the SMR similarly to the vibration amplitude (Fig. 1c, Supplementary Fig. 1 and Supplementary Video 1). Positioning a particle at the node changes the acoustic velocities (Fig. 1c, inset and Supplementary Video 2). When we calculated the resonant frequency shift by integrating the acoustic energy terms obtained from the simulation (Supplementary Tables 1, 2 and Supplementary Note 2), we obtained excellent agreement ( $R^2=0.984$ ) with our measurements (Fig. 1d). We confirmed that the particle-fluid density difference has negligible effect on node deviation (Supplementary Fig. 2). To validate that acoustic effects can be measured independently of buoyant mass, we measured a bead in a density-matched fluid ( $\rho_{\text{fluid}} = \rho_{\text{bead}}$ ). This resulted in zero resonant frequency shift at the antinode ( $\Delta f/f|_{\text{antinode}} = 0$ ), but a noticeable resonant frequency shift at the node in both the experiment and simulation, which showed

excellent agreement with each other ( $R^2=0.994$ , Fig. 1e). Additional measurements revealed that node deviation is independent of fluid velocity or vibration amplitude (Supplementary Fig. 3a,b). Therefore, by measuring the resonant frequency shift at the node and antinode as cells flow through the SMR, it is possible to simultaneously and independently quantify the acoustic scattering and buoyant mass of the cell (Fig. 1a, bottom).

We compared polystyrene particles with different volumes and observed that node deviation changes with particle volume (Fig. 1f). The volume dependence can be accounted for by utilizing the buoyant mass measurement. To establish the correlation between node deviation and stiffness, we fabricated hydrogels with varying elastic modulus by changing their chemical composition and characterized the elastic modulus of the hydrogels using AFM. When measuring the mechanical properties with the SMR, we observed that the node deviation of the hydrogels increases monotonically with their elastic modulus over the range 0.1-100kPa (Fig. 1g). We also observed that node deviation is not sensitive to particle shape for hydrogels of the same elastic modulus and aspect ratios in the range of 1-2.5 (Supplementary Fig. 3c).

### **Size-normalized acoustic scattering (SNACS) depends on cell cortex mechanical properties.**

Next, we asked if mechanical properties of live cells could be probed by measuring node deviation. We implemented the 'Cortical Shell – Liquid Core' model<sup>25</sup> in our FEM simulation (Fig. 2a), which highlights the role of actomyosin cortex in cell mechanics<sup>26,27</sup>. We calculated that the acoustic interactions caused relatively small deformations (<15 nm) on the cell surface (Supplementary Note 2), suggesting that node deviation may be primarily governed by the actomyosin cortex<sup>28</sup>. We then compared our FEM simulations with the node deviation of mouse lymphoblast (L1210) cells (Fig. 2b). FEM simulations yielded similar range signals to the experiments when we used an elastic modulus of 4-8 MPa for the cortex (Fig. 2b), which is 1-2 orders of magnitude higher than the previously reported value using AFM<sup>27,28</sup>. This is likely due to the high frequency of our mechanical measurement ( $\sim 1$  MHz) compared to the conventional frequency range of AFM operation (1-100 Hz) and a power-law relationship between apparent elastic modulus ( $E$ ) and the frequency ( $f$ ):  $E \propto f^{0.2-0.3}$ <sup>29</sup>. Consistent with our results, a similar value was reported with other high-frequency stiffness measurements of red blood cells<sup>30</sup>. Next, to correct for cell size dependence of the node deviation measurement (Fig. 1f), we derived a size-independent acoustic scattering parameter from the iso-elasticity lines obtained from the FEM simulations (Fig. 2b, Supplementary Fig. 4). We called this the size-normalized acoustic scattering, SNACS (Fig. 2b). The iso-elasticity lines fit well with the measurements from hundreds of live cells. The FEM simulations indicated that SNACS increases with

elastic modulus of the cortex ( $E_{mod}$ , Fig. 2b, inset) as well as with cortical thickness ( $t_s$ ), but is insensitive to both intracellular pressure and cortical tension (Supplementary Fig. 5). We also tested three other mechanical models but none of them matched well with our observations (Supplementary Table 3). These results are consistent with previous observations showing small deformation primarily probes mechanical properties of the cell cortex [refs].

To experimentally validate whether SNACS correlates with mechanical properties of live cells, we examined SNACS upon chemical perturbations. All actomyosin inhibitors tested decreased SNACS (Fig. 2c). We also generated a L1210 cell line that stably expresses the LifeAct-RFP F-actin probe<sup>31</sup>. We imaged these cells and observed that the chemical inhibitors of actin polymerization caused either a punctured cortex (Latrunculin B) or polarized cortex (Cytochalsin D) (Fig. 2d). Both of these cortex phenotypes yielded a reduction in SNACS (Fig. 2c), substantially more than our system noise (Supplementary Fig. 6). We also observed a reduced SNACS after microtubule perturbing Nocodazole treatment, but this treatment also affected the actin cortex morphology (Supplementary Fig. 7). The opposite change in SNACS was observed when we cross-linked cellular structures using a 1-10 min exposure to 4% Paraformaldehyde (Fig. 2e). Moreover, when we osmotically perturbed cells, SNACS changed with the applied osmotic pressure (Fig. 2f). Importantly, these perturbations resulted in SNACS changes (Figs. 2c-f) that are consistent with previous experiments where stiffness was measured by a wide range of methods<sup>9,10,13,14,32,33</sup>. Thus, taken together with the hydrogel results (Fig. 1g) and our FEM simulation results, SNACS measures stiffness and especially the stiffness of the cell cortex.

### **SNACS remains stable during interphase but is dynamic during mitosis**

Next, we asked if both SNACS and buoyant mass of the same cell could be repeatedly measured throughout the cell cycle. To do this, we implemented a previously reported fluidic control strategy that enables continuous, non-invasive SMR measurements of the same cell<sup>34</sup>. We simultaneously measured SNACS and buoyant mass of the same cell over multiple generations (Fig. 3a). Interdivision times measured in the SMR during the SNACS measurements were unchanged from bulk culture (Supplementary Fig. 8), suggesting that our measurement is not invasive. We observed that individual cells display stable SNACS throughout the interphase, exhibiting significantly lower variability than what is seen across different cells in interphase (Fig. 3b). This suggests that cell-to-cell variability in cell mechanical properties during interphase does not arise from cell cycle dependent variability, but rather from mechanical differences that accumulate over generations.

In contrast to interphase, mitotic cells displayed large changes in SNACS (Fig. 3c). Employing on-chip microscopy to acquire Differential Interference Contrast (DIC) images, we imaged the morphology of the cell to pinpoint the onset of anaphase (Fig. 3d), and correct for mass elongation effects on the SNACS measurement during anaphase and telophase (Supplementary Fig. 9, Supplementary Table 4 and Supplementary Notes 3, 4). SNACS decreased gradually during early mitosis, but not in G2, and abruptly increased at the onset of anaphase followed by a rapid decrease and recovery (Fig. 3c and Supplementary Fig. 10a,b). The error in the SNACS measurement increased after cells became full doublets (~15 min after the onset of anaphase), making subsequent SNACS changes until division not statistically significant ( $P > 0.05$ ; two-sided Welch's t-test, Fig. 3c). Although the duration and magnitude of the SNACS dynamics varied in other mammalian cells (Fig. 3e,f), we observed similar trends.

### **Mitotic swelling is responsible for SNACS decrease in early mitosis**

Given that SNACS scales inversely with swelling (Fig. 2f), we hypothesized that mitotic swelling occurring in prophase and metaphase<sup>35,36</sup> might be responsible for the gradual decrease in SNACS. To test this hypothesis, we first correlated the timing of the mitotic swelling and SNACS change by simultaneously measuring SNACS and cell volume. Briefly, we consecutively weighed cells in two fluids of different densities during each cycle in order to derive single-cell volume, density and mass using a previous technique<sup>36</sup>. By combining this technique with the SNACS measurement, we observed that the SNACS decreases concomitantly with mitotic swelling (Fig. 4a). We further validated this by arresting cells in metaphase, where mitotic swelling is at a maximum<sup>36</sup>, using the kinesin inhibitor S-trityl-L-cysteine (STLC). Upon mitotic entry, STLC treated cells displayed similar change in SNACS to that seen during mitotic swelling of untreated cells (Fig. 4b, c). However, with STLC treatment, SNACS remained low for several hours (Fig. 4b). These results suggest that SNACS decreases concomitantly with mitotic swelling during prophase and metaphase, and further confirm that the subsequent increase in SNACS happens after metaphase.

We next acquired causative evidence that mitotic swelling causes the reduction in SNACS during prophase and metaphase. Previously we showed that inhibiting the Na<sup>+</sup>/H<sup>+</sup> antiporter with ethylisopropylamide (EIPA) reduces mitotic swelling without inhibiting mitosis<sup>36</sup>. Here, we found that upon EIPA treatment, SNACS in early mitosis was no longer reduced to the same extent as in the control cells and cells arrested in metaphase (Fig. 4c and Supplementary Fig. 10c).  $\Delta$ SNACS of EIPA treated cells in early mitosis was  $-0.08 \pm 0.02$  ( $n = 5$  cells, all values are mean  $\pm$  s.e.m. unless stated otherwise) whereas  $\Delta$ SNACS of control cells and cells arrested in metaphase were  $-0.22 \pm 0.01$  ( $n =$

24 cells) and  $0.24 \pm 0.03$  ( $n = 7$  cells), respectively. These suggest that mitotic swelling is largely responsible for the reduction in SNACS. To determine if swelling without a mitotic event can decrease SNACS, we induced swelling with a hypotonic shock ( $-\Delta 50$  mOsm) in non-mitotic (interphase) cells. Immediately after the osmotic shock, cells swelled by  $\sim 15\%$  in volume, as normally observed in mitotic swelling<sup>36</sup>, and SNACS was reduced by a similar magnitude ( $\Delta$ SNACS =  $-0.18 \pm 0.01$ ,  $n = 733$  cells) to that seen during mitotic swelling (Fig. 4d). To mimic the gradual swelling during mitosis and potentially prevent membrane detachment from the cortex<sup>32</sup>, we compared fast and slow swelling ( $-\Delta 50$  mOsm instantaneously or over 20 minutes) and the swelling rate did not affect the SNACS decrease (Supplementary Fig. 11). We hypothesized that swelling reduces cortical thickness by hydrostatic pressure, thereby expanding actin to cover a larger surface area (Supplementary Note 5). We estimated that swelling of  $\sim 15\%$  would lead to  $\sim 10\%$  cortex thickness decrease assuming that the amount of cortical actin does not change during swelling (Supplementary Table 5). We used live cell fluorescent microscopy and showed that the cortex thickness gradually decreased during mitotic swelling by an amount similar to our calculation ( $\sim 10\%$ ) after nuclear envelope breakdown but before the onset of anaphase (Supplementary Figs. 12 and 13), consistent with previous studies<sup>1,37</sup>. Altogether, these data suggest that mitotic swelling is responsible for cortical thinning and consequent decrease in SNACS.

### **SNACS reveals mechanical changes during actin remodeling in late mitosis**

We investigated the rapid SNACS change during anaphase and telophase (Fig. 3c). First, we observed that the SNACS increase in early anaphase (Fig. 4a, c, red) was not present in EIPA treated samples (Fig. 4c, blue and Supplementary Fig. 10c), suggesting that the SNACS increase represents recovery from mitotic swelling. To link mechanical dynamics to actin remodeling, we imaged changes in actin cortex distribution during anaphase and telophase (Fig. 4e and Supplementary Fig. 14). In early anaphase ( $\sim 5$  min after onset of anaphase) where SNACS initially increases, cells started to elongate and the cleavage furrow was initiated. At approximately 10 min into anaphase, where SNACS decreased, cells redistributed their cortical actin out of the polar regions. This polar relaxation<sup>2</sup> caused a 10-15% depletion in F-actin at the poles and lasted approximately 5 min (Fig. 4f and Supplementary Fig. 12i-l). Both SNACS and polar relaxation were recovered approximately 15 min after the onset of anaphase (Fig. 4f). When we inhibited cytokinesis and actin remodeling using the myosin II motor inhibitor Blebbistatin, cells still displayed a gradual SNACS decrease in early mitosis caused by mitotic swelling, but the mechanical dynamics in anaphase and telophase observed in untreated cells disappeared (Fig. 4g). These observations reveal how cortical thinning induced by

mitotic swelling in early mitosis and actin remodeling, especially polar relaxation, in late mitosis result in dynamic changes in cellular mechanical properties (Fig. 4h).

## Discussion

During early mitosis where SNACS decreases, it is known that cells exhibit swelling, the actin cortex thickness is reduced and cortical tension is increased<sup>1,37</sup>, yet prior work on how stiffness changes has not been consistent. Previously it has been thought that mitotic cells become stiffer due to increased tension<sup>40</sup> from contractility in the membrane during mitotic round up. Early AFM<sup>41</sup> and optical tweezer<sup>39</sup> results on cells in mitosis supported this notion. The observed SNACS decrease we observe could result from the reduction in both cortex thickness and modulus. However, a separate report using AFM found no change in mitotic stiffness<sup>42</sup>, whereas others using hydrodynamic forces have observed mitotic cells being more deformable<sup>43</sup>. All of these studies<sup>39,41-43</sup> were conducted as endpoint assays on different cell types with strains that were 10 to 100-fold larger than those used during our SNACS measurement. Future work will be necessary to determine how the cortex tension, modulus and thickness govern cell stiffness dynamics during mitosis. Aside from the cortex, it remains plausible that SNACS reflects other attributes of the cell such as the plasma membrane and the way in which it is attached to the underlying cortex.

We also found that at the onset of anaphase, SNACS first recovers from cell swelling and then reduces again during anaphase and telophase. Early work on mechanical properties of sea urchin eggs suggested similar dynamic changes in anaphase<sup>44</sup>. This second reduction in SNACS was dependent on actomyosin remodeling and coincided with the polar relaxation of actin cortex<sup>2</sup>.

Finally, our SNACS measurement is influenced by the cell's mass distribution along the cantilever. During anaphase and telophase, the cell's mass distribution changes substantially, which causes the SNACS measurement to depend on the cell's orientation within the channel (Supplementary Fig. 15, Supplementary Note 4 and Supplementary Table 4). Therefore, obtaining mechanical measurements by acoustic scattering requires mass distribution information through bright-field images unless cell shape is known a priori. In round interphase cells, such as the ones we have studied here, this correction is not required.

We show that measuring single-cell mechanical properties continuously, with high temporal resolution over extended periods is critical for observing small changes which are both transient and asynchronous between cells. We demonstrate this by measuring mitotic-specific mechanical changes



that are smaller than the population variance and occur within minute timescales. Importantly, our SNACS measurement quantifies the overall mechanical properties of a cell, complementing spatially resolved measurements such as time-lapse microscopy, traction force microscopy and atomic force microscopy.

## Acknowledgements

We would like to thank K. Elias (Brigham and Women's Hospital) for S-Hela and E. Vasile and the Koch Institute microscopy core, which is partly funded by the Koch Institute Support Grant P30-CA14051 from the National Cancer Institute, for technical support. This work was funded in part by the Ludwig Center for Molecular Oncology (S.R.M.), Cancer Systems Biology Consortium U54 CA217377 from the NCI (S.R.M.), Institute for Collaborative Biotechnologies through grant W911NF-09-0001 from the US Army Research Office (S.R.M.). T.P.M. is supported by the Wellcome Trust Sir Henry Postdoctoral Fellowship grant 110275/Z/15/Z and J.H.K. acknowledges support from Samsung scholarship.

## Author contributions

J.H.K. and S.R.M. conceptualized the study. J.H.K., with assistance from S.O., G.K. and S.R.M., designed the modelling and experiments done with beads. J.H.K. and T.P.M. designed the experiments with cells. J.H.K. performed all node deviation experiments and analyzed the data. J.H.K., with assistance from G.K., carried out the modelling. T.P.M. carried out all imaging experiments. S.O., with assistance from J.H.K. and T.P.M., carried out the image analysis. L.C. and P.S.D. created the hydrogel particles. T.P.M. and S.R.M. supervised the study. J.H.K., T.P.M, G.K. and S.R.M. wrote the paper with input from all authors.

## Competing interests

S.R.M. is a founder of Travera and Affinity Biosensors. The other authors declare no competing interests.

## References

- 1 Chugh, P. *et al.* Actin cortex architecture regulates cell surface tension. *Nat Cell Biol* **19**, 689-697 (2017).
- 2 Rodrigues, N. T. *et al.* Kinetochores-localized PP1-Sds22 couples chromosome segregation to polar relaxation. *Nature* **524**, 489-492 (2015).
- 3 Fletcher, D. A. & Mullins, R. D. Cell mechanics and the cytoskeleton. *Nature* **463**, 485-492 (2010).
- 4 Gardel, M. L., Schneider, I. C., Aratyn-Schaus, Y. & Waterman, C. M. Mechanical integration of actin and adhesion dynamics in cell migration. *Annu Rev Cell Dev Biol* **26**, 315-333 (2010).
- 5 Byun, S. *et al.* Characterizing deformability and surface friction of cancer cells. *Proceedings of the National Academy of Sciences of the United States of America* **110**, 7580-7585 (2013).

- 6 Swaminathan, V. *et al.* Mechanical stiffness grades metastatic potential in patient tumor cells and in cancer cell lines. *Cancer Res* **71**, 5075-5080 (2011).
- 7 Paluch, E. & Heisenberg, C. P. Biology and physics of cell shape changes in development. *Curr Biol* **19**, R790-799 (2009).
- 8 Henderson, E., Haydon, P. G. & Sakaguchi, D. S. Actin filament dynamics in living glial cells imaged by atomic force microscopy. *Science* **257**, 1944-1946 (1992).
- 9 Radmacher, M. Studying the mechanics of cellular processes by atomic force microscopy. *Methods Cell Biol* **83**, 347-372 (2007).
- 10 Ou-Yang, H. D. & Wei, M. T. Complex fluids: probing mechanical properties of biological systems with optical tweezers. *Annu Rev Phys Chem* **61**, 421-440 (2010).
- 11 Wang, N., Butler, J. P. & Ingber, D. E. Mechanotransduction across the cell surface and through the cytoskeleton. *Science* **260**, 1124-1127 (1993).
- 12 Lincoln, B., Wottawah, F., Schinkinger, S., Ebert, S. & Guck, J. High-throughput rheological measurements with an optical stretcher. *Methods Cell Biol* **83**, 397-423 (2007).
- 13 Gossett, D. R. *et al.* Hydrodynamic stretching of single cells for large population mechanical phenotyping. *Proceedings of the National Academy of Sciences of the United States of America* **109**, 7630-7635 (2012).
- 14 Otto, O. *et al.* Real-time deformability cytometry: on-the-fly cell mechanical phenotyping. *Nat Methods* **12**, 199-202, 194 p following 202 (2015).
- 15 Brangwynne, C. P., MacKintosh, F. C. & Weitz, D. A. Force fluctuations and polymerization dynamics of intracellular microtubules. *Proceedings of the National Academy of Sciences of the United States of America* **104**, 16128-16133 (2007).
- 16 Gupta, S. K. & Guo, M. Equilibrium and out-of-equilibrium mechanics of living mammalian cytoplasm. *Journal of the Mechanics and Physics of Solids* **107**, 284-293 (2017).
- 17 Tseng, Y., Kole, T. P. & Wirtz, D. Micromechanical mapping of live cells by multiple-particle-tracking microrheology. *Biophysical journal* **83**, 3162-3176 (2002).
- 18 Matzke, R., Jacobson, K. & Radmacher, M. Direct, high-resolution measurement of furrow stiffening during division of adherent cells. *Nat Cell Biol* **3**, 607-610 (2001).
- 19 Guillou, L., Babataheri, A., Puech, P. H., Barakat, A. I. & Husson, J. Dynamic monitoring of cell mechanical properties using profile microindentation. *Sci Rep* **6**, 21529 (2016).
- 20 Wang, H. *et al.* Acoustophoretic force-based compressibility measurement of cancer cells having different metastatic potential. 045019-045019 (2013).
- 21 Yang, T. *et al.* A comprehensive strategy for the analysis of acoustic compressibility and optical deformability on single cells. *Sci Rep* **6**, 23946 (2016).
- 22 Hartono, D. *et al.* On-chip measurements of cell compressibility via acoustic radiation. *Lab Chip* **11**, 4072-4080 (2011).
- 23 Burg, T. P. *et al.* Weighing of biomolecules, single cells and single nanoparticles in fluid. *Nature* **446**, 1066-1069 (2007).
- 24 Dohn, S., Svendsen, W., Boisen, A. & Hansen, O. Mass and position determination of attached particles on cantilever based mass sensors. *The Review of scientific instruments* **78**, 103303 (2007).
- 25 Yeung, A. & Evans, E. Cortical shell-liquid core model for passive flow of liquid-like spherical cells into micropipets. *Biophysical journal* **56**, 139-149 (1989).
- 26 Lim, C. T., Zhou, E. H. & Quek, S. T. Mechanical models for living cells--a review. *J Biomech* **39**, 195-216 (2006).
- 27 Fischer-Friedrich, E. *et al.* Rheology of the Active Cell Cortex in Mitosis. *Biophysical journal* **111**, 589-600 (2016).

- 28 Cartagena-Rivera A , X., Logue J , S., Waterman C , M. & Chadwick R , S. Actomyosin Cortical Mechanical Properties in Nonadherent Cells Determined by Atomic Force Microscopy. *Biophysical journal* **110**, 2528-2539 (2016).
- 29 Balland, M. *et al.* Power laws in microrheology experiments on living cells: Comparative analysis and modeling. *Physical review. E, Statistical, nonlinear, and soft matter physics* **74**, 021911 (2006).
- 30 Wang, A., Vijayraghavan, K., Solgaard, O. & Butte, M. J. Fast Stiffness Mapping of Cells Using High-Bandwidth Atomic Force Microscopy. *ACS Nano* **10**, 257-264 (2016).
- 31 Riedl, J. *et al.* Lifeact: a versatile marker to visualize F-actin. *Nat Methods* **5**, 605-607 (2008).
- 32 Steltenkamp, S., Rommel, C., Wegener, J. & Janshoff, A. Membrane stiffness of animal cells challenged by osmotic stress. *Small* **2**, 1016-1020 (2006).
- 33 Guo, M. *et al.* Cell volume change through water efflux impacts cell stiffness and stem cell fate. *Proceedings of the National Academy of Sciences of the United States of America* (2017).
- 34 Son, S. *et al.* Direct observation of mammalian cell growth and size regulation. *Nat Methods* **9**, 910-912 (2012).
- 35 Zlotek-Zlotkiewicz, E., Monnier, S., Cappello, G., Le Berre, M. & Piel, M. Optical volume and mass measurements show that mammalian cells swell during mitosis. *J Cell Biol* **211**, 765-774 (2015).
- 36 Son, S. *et al.* Resonant microchannel volume and mass measurements show that suspended cells swell during mitosis. *J Cell Biol* **211**, 757-763 (2015).
- 37 Ramanathan, S. P. *et al.* Cdk1-dependent mitotic enrichment of cortical myosin II promotes cell rounding against confinement. *Nat Cell Biol* **17**, 148-159 (2015).
- 38 Ananthakrishnan, R. *et al.* Quantifying the contribution of actin networks to the elastic strength of fibroblasts. *J Theor Biol* **242**, 502-516 (2006).
- 39 Matthews, H. K. *et al.* Changes in Ect2 localization couple actomyosin-dependent cell shape changes to mitotic progression. *Dev Cell* **23**, 371-383 (2012).
- 40 Stewart, M. P. *et al.* Hydrostatic pressure and the actomyosin cortex drive mitotic cell rounding. *Nature* **469**, 226-230 (2011).
- 41 Kunda, P., Pelling, A. E., Liu, T. & Baum, B. Moesin controls cortical rigidity, cell rounding, and spindle morphogenesis during mitosis. *Curr Biol* **18**, 91-101 (2008).
- 42 Jiang, N. *et al.* Probing the biophysical properties of tumor cells during mitosis by atomic force microscopy. *Biomech Model Mechanobiol* **17**, 1209-1215 (2018).
- 43 Rosendahl, P. *et al.* Real-time fluorescence and deformability cytometry. *Nat Methods* **15**, 355-358 (2018).
- 44 Hiramoto, Y. Mechanical properties of the surface of the sea urchin egg at fertilization and during cleavage. *Exp Cell Res* **89**, 320-326 (1974).
- 45 Clark, A. G., Dierkes, K. & Paluch, E. K. Monitoring actin cortex thickness in live cells. *Biophysical journal* **105**, 570-580 (2013).

## Figure legends

**Figure 1. Acoustic scattering causes a resonant frequency shift at the node of a suspended microchannel resonator (SMR).** **a**, Top, schematic of SMR with a particle flowing through the embedded fluidic channel. Pink arrows mark the particle trajectory. Middle, normalized vibration amplitude at the 2<sup>nd</sup> mode. Bottom, resonant frequency shift ( $\Delta f/f$ ) from experiments with a single cell (pink) and a polystyrene bead (black). Vertical dotted lines mark the particle positions along the cantilever, as in top panel. Buoyant mass (size) is measured at the antinode ( $\Delta f/f|_{\text{antinode}}$ , blue arrow). Inset,  $\Delta f/f$  at the node where node deviation is measured ( $\Delta f/f|_{\text{node}}$ , black and pink arrows). **b**, Conceptual illustration of frequency shift due to acoustic scattering. A particle interacts with acoustic fields (black waves) generated by the SMR vibration (black arrows) at resonant frequency  $f$ . The particle-fluid interaction causes acoustic scattering (blue waves), which shifts the resonant frequency ( $\Delta f$ ). The wavelength ( $\lambda$ ) of the acoustic fields is depicted qualitatively ( $\lambda \sim 1$  mm, which is  $\sim 100$  times the channel height). **c**, Acoustic pressure (colors) and acoustic velocities (arrows) within SMR from Finite Element Method simulations. Inset, magnitudes of y-acoustic velocities with and without a polystyrene bead at the node. Black arrows show directions of y-acoustic velocities. **d**, **e**,  $\Delta f/f$  from simulations (red circles) and experiments (black lines) with polystyrene beads flowing through SMR filled with H<sub>2</sub>O (**d**) or density-matched fluid ( $\rho_{\text{bead}} = \rho_{\text{fluid}}$ ) (**e**). Black arrows show node deviation. **f**, Node deviation vs particle volume from simulations (red dashed line) and experiments (black dots) with polystyrene beads. **g**, Node deviation vs mean elastic modulus, as measured using AFM indentation (Methods), for synthetic hydrogels of same volume (n=92, 115, 243, 146, 134 and 186 hydrogels for node deviation measurements, n=4 hydrogels for each AFM measurements). Data depicts mean (blue squares)  $\pm$  s.d. (error bars).

**Figure 2. Size-normalized acoustic scattering (SNACS) measures changes in mechanical properties of cells.** **a**, Schematic of ‘Cortical Shell – Liquid Core’ model, where  $E_{\text{mod}}$  is the elastic modulus of a shell. Cortical thickness ( $t_s$ ) was set to 2% of the cell radius ( $r_c$ )<sup>45</sup>. **b**, Node deviation (volume-normalized) vs volume  $V$  from experiments with L1210 cells (black dots) and simulations using the model for three values of cortical elastic modulus ( $E_{\text{mod}}$ , 4, 6 and 8 MPa, color lines). Vertical offsets of iso-elasticity lines define SNACS (Methods). Inset,  $\Delta f/f$  from simulations with different cortical elastic modulus (4, 6 and 8 MPa,  $V = 900$  fL). **c**, SNACS obtained from L1210 cells treated with inhibitors of actomyosin cortex: Latrunculin B (LatB, 0.02, 0.1, 0.4 and 1  $\mu\text{M}$ , n = 381, 385, 346 and 383 cells, respectively,  $P = 0.036, 3.8 \times 10^{-5}, 1.03 \times 10^{-8}$  and  $4.5 \times 10^{-18}$ , respectively), Cytochalasin D (CytoD, 1  $\mu\text{M}$ , n = 332 cells,  $P = 1.2 \times 10^{-8}$ ), and Blebbistatin (Bleb, 50  $\mu\text{M}$ , n = 349 cells,  $P = 0.023$ ). Statistical comparisons (two-sided Welch’s t-test) were made to DMSO control (0.1 %, n = 337 cells). **d**, Representative single z-layer images of F-actin (LifeAct) from live L1210 cells before and after 1  $\mu\text{M}$  LatB (n = 9 fields of views) and 1  $\mu\text{M}$  CytoD (n = 12 fields of views) treatment. Scale bars, 10  $\mu\text{m}$ . **e**, SNACS of L1210 cells after crosslinking with 4% Paraformaldehyde (PFA, 1 and 10 min exposure, n=247 and 367 cells, respectively,  $P = 2.0 \times 10^{-56}$  and  $6.7 \times 10^{-175}$ , respectively). Statistical comparisons (two-sided Welch’s t-test) were made to DMSO control (0.1 %, n = 1047 cells). **f**, Effect of osmotic stress on SNACS. Cells were resuspended in hypo- (200 mOsm, n = 611 cells,  $P = 2.9 \times 10^{-10}$ ) or hyperosmotic (350, 400 and 500 mOsm, n = 544, 571 and 574 cells, respectively,  $P = 8.1 \times 10^{-65}, 2.6 \times 10^{-144}$  and  $< 10^{-200}$ , respectively) media. Statistical comparisons (one-way ANOVA, Fisher’s LSD) were made to iso-osmotic (300 mOsm, n = 539 cells) media. In **c,e,f**, boxes: interquartile range, squares: mean, whiskers: 5-95%, horizontal dashed lines: mean SNACS of control (DMSO or 300 mOsm); \* $P < 0.05$ , \*\*\*\* $P < 0.0001$ .

**Figure 3. Continuous monitoring of single-cell SNACS throughout the cell cycle.** **a**, Top, buoyant mass (black) and SNACS (red) of a L1210 cell was measured over two cell divisions with < 1 min temporal resolution by flowing the cell back-and-forth through the SMR. Blue arrows mark cell division. Bottom, SNACS near mitosis. SNACS is shown in dashed lines when measurement error becomes statistically significant (Methods). **b**, SNACS variability during interphase at a cell population level (black), in individual cells (red), and for 12  $\mu\text{m}$  polystyrene beads (blue). Bead SNACS is relative to its mean value. Large (mitotic) cells were removed from the population data.  $\langle C.V \rangle$  is the average coefficient of variation.  $n$  is the number of cells (black) or beads (blue) measured from each population and the number of repeated measurements during interphase of each individual cell (red) or bead (blue). Boxes:  $\pm$  s.d., squares: mean, whiskers: 5-95%. **c**, mean SNACS (red) and  $\pm$  s.d. (gray) of L1210 cells during mitosis ( $n = 24$  cells from 13 independent experiments). Vertical lines and color bars indicate the phase of the cell cycle. Short blue lines at the bottom right mark the end of cell division for each cell. Dashed line same as in **a**. **d**, Representative morphology of a L1210 cell ( $n = 24$  cells from 13 independent experiments) captured by DIC imaging on the SMR chip. Numbering corresponds to arrows in **c**. Scale bars, 10  $\mu\text{m}$ . **e,f**, SNACS in mammalian cells BaF3 (**e**) and S-Hela (**f**). Color bars same as in **c**.

**Figure 4. Mitotic swelling and actin remodeling are responsible for SNACS dynamics in mitosis.** **a**, L1210 cell volume (blue circles) and SNACS (red) in mitosis. **b**, Buoyant mass (black) and SNACS (red) of a L1210 cell arrested in metaphase by treating with S-trityl-cysteine (STLC, 5  $\mu\text{M}$ ). **c**, Left, mean SNACS change of control (red) and ethylisopropylamiloride (EIPA, 10  $\mu\text{M}$ ) treated L1210 cells in early mitosis. Right, quantification of SNACS change with STLC (5  $\mu\text{M}$ ,  $n = 7$  cells from 7 independent experiments,  $P = 0.58$ ) and EIPA (10  $\mu\text{M}$ ,  $n = 5$  cells from 5 independent experiments.  $P = 3.0 \times 10^{-5}$ ) treatments. Data depicts mean  $\pm$  s.d. of the maximal SNACS change in prophase and metaphase. Statistical comparisons (two-sided Welch's t-test) were made to the control ( $n = 24$  cells from 13 independent experiments). \*\*\*\* $P < 0.0001$ , n.s., not significant. **d**, Top, illustration of hypothetical cortical thinning scenario by shell expansion during swelling (Supplementary Note 5). Bottom, SNACS of L1210 cells vs time before (red,  $n = 728$  cells) and after ( $-\Delta 50$  mOsm, blue,  $n = 733$  cells) exposure to hypotonic stress. Dashed lines represent the mean SNACS of each condition. Arrow marks the time of osmotic shock. **e**, Representative single z-layer images of F-actin (red, LifeAct) and FUCCI (green, mAG-hGem) from a live L1210 cell ( $n = 7$  cells). Time zero marks the onset of anaphase. Furrow initiation in the equatorial region (pink arrowheads) and cortical relaxation at the poles (blue arrows) are highlighted. Scale bars, 10  $\mu\text{m}$ . **f**, Top, zoom-in view of mean SNACS in late mitotic L1210 cells ( $n = 24$  cells). Bottom, L1210 cortical LifeAct signal density in equatorial (red) and polar (blue) regions (Methods), as shown in **e**. Data depicts mean  $\pm$  s.d. ( $n = 7$  cells). **g**, Buoyant mass (black) and SNACS (red) of a L1210 cell treated with Blebbistatin (Bleb, 25  $\mu\text{M}$ ). **h**, Summary of SNACS dynamics in mitosis. Data depicts mean  $\pm$  s.d. of the SNACS normalized to G2 ( $n = 24$  cells). Actin (gray shell) and morphology of a cell in each time points of mitosis are illustrated. In **a,b,c,f,g**, vertical lines separate the cell cycle positions marked by color bars shown in Fig. 3c. Black bar marks post-metaphase. P: prophase, M: metaphase, A: anaphase, T: telophase, post-M: post-metaphase.

## Online methods

### System Setup

SMR devices were fabricated using a previously described process<sup>23,46</sup> and carried out at CEA-LETI, Grenoble, France. The geometry and dimensions of SMR devices used in the experiments described in this work are shown in Supplementary Fig. 1 and Supplementary Table 2. The measurement system for trapping a cell throughout its cell cycle has been previously described in<sup>34</sup>. The SMRs were vibrated with a piezo-ceramic plate bonded underneath the chip, providing actuation to resonate the cantilever beam in the second mode. To track the changes in the resonant frequency of the cantilever as a function of time, we used a closed feedback loop to drive the cantilever to always oscillate at its resonant frequency. The motion of the cantilever was measured using piezoresistors that are implanted at the base of the silicon cantilever<sup>47</sup>. A digital control platform that was previously reported<sup>48</sup> was utilized to oscillate the SMR in direct feedback mode, where the motion signal acquired from the piezoresistor is delayed, amplified and utilized as the drive signal used to actuate the cantilever. We set the measurement bandwidth of this control system at  $\sim 1,500$  Hz, which is wide enough to capture frequency modulation signals created by cell transit events and narrow enough to minimize noise.

For on-chip optical measurements, a modular microscope (Nikon) was mounted on top of the SMR device. A 20X objective lens (Nikon-CFI, LU Plan ELWD N.A. 0.4 WD 13 mm) or 50X objective lens (Nikon-CFI, LU Plan ELWD N.A. 0.55, W.D 10.1 mm) was used to collect light into a CMOS camera (FLIR, BFS-U3-13Y3M-C) or PMT (Hamamatsu, H10722-20), respectively, in order to obtain DIC images or measure fluorescent intensity. The field of view and area of light exposure was typically reduced to  $100\ \mu\text{m} \times 100\ \mu\text{m}$  (DIC imaging) or  $40 \times 60\ \mu\text{m}$  (fluorescent measurements) to minimize the background noise as well as phototoxicity. To further improve the signal-to-noise ratio, a rectangular slit (Thorlab) was adjusted to fit the channel width and placed at the image plane. An illumination light source (Lumencor, Spectra X Light Engine) was shuttered by the measurement software (Labview 2012) to excite each fluorescent measurement for less than 550 ms. The optical path and components for imaging and fluorescent measurements are similar to what has been previously described<sup>34</sup>.

### System Operation

As previously reported<sup>36</sup>, a chip was placed on top of a hollow copper plate that is connected to a water bath by tubing to maintain constant temperature on the chip. For all single-cell, long-term monitoring experiments, temperature of the copper plate was kept at  $37^\circ\text{C}$ . The sample was loaded to the SMR from vials pressurized with air containing 5%  $\text{CO}_2$  to maintain the pH of the culture. A 0.007" inner diameter fluorinated ethylene propylene (FEP) tubing (IDEX Health & Science) is utilized to push the sample into the chip. The fluid flow was controlled using two electronic pressure regulators (Proportion Air QPV1) and three solenoid valves (SMC-S070), which are controlled by National Instruments control cards and a custom measurement software (Labview 2012). Typically, differential pressure of  $\sim 0.5$  psi was applied across the SMR, yielding a flow rate of  $\sim 2$  nL/s (calculated based on the frequency modulation signal due a cell transit; typically 200-300 ms) to maintain constant shear and data rate. Under these conditions, the L1210 cell growth rate was similar to that in culture<sup>34</sup>. Beads, hydrogels and drug-response end-point assays were measured at room temperature. All end-point assays were conducted within 30 min after samples were loaded. New samples were flushed every several minutes into the input bypass to minimize potential size bias due to particle or cell settling in the tubing and sample vials.

### Frequency peak analysis

To measure buoyant mass (antinode) and node deviation (node) from the acquired resonant frequency waveforms, we filtered the frequency data with a third order Savitzky-Golay low-pass filter

and find the local minima (antinode) that is below a user-defined threshold. Next, local maxima (node) around the peaks were determined. Then to correct for the possible slope during the particle or cell transition through the cantilever, a baseline was calculated and subtracted from the measured peaks by fitting a first order polynomial at frequency data points prior and posterior of the cell signal. Typically, we acquire frequency data for  $\sim 1$  s before and after the transit of each cell in order to estimate the baseline frequency. As a result, the measurement time is typically 2-3 s per cell which leads to a throughput of about 1,200 cells per hour (accounting for occasional doublets and delays between cell measurements). For single-cell volume measurements (Fig. 4a), baselines were fitted with 2<sup>nd</sup> order polynomial to account for the baseline fluctuation due to fluid exchange. Both local maxima and minima in the cell signal were subtracted from the linear baseline to obtain the buoyant mass (local minima, antinode) and node deviation (local maxima, node). For single-cell end-point assays (population measurements), frequency peaks were rejected when local minima (two antinodes) differed from each other more than 10% of the average value and/or local maxima (two nodes) differed from each other more than 15% of the average value of local minima, which occur when multiple cells or cell with debris enter the SMR simultaneously. Peaks were rejected if their shape was atypical (e.g. particle or cell stuck in the cantilever). For single-cell long-term monitoring, all frequency peaks were accepted and presented except extremely rare events such as when a doublet separated into two daughter cells during the transit through the cantilever or entered apoptosis due to persistent drug pressure. Frequency peaks were calibrated (*Hz per pg*) using monodisperse 10  $\mu\text{m}$  diameter polystyrene beads with a known density of 1.05  $\text{g}/\text{cm}^3$  (Thermofisher, Duke Standards).

### Hydrogel particle synthesis

Hydrogel microparticles were fabricated via stop-flow lithography (SFL)<sup>49,50</sup>. Microfluidic synthesis devices were fabricated by previously reported procedures.<sup>2</sup> Briefly, PDMS (10:1 monomer to curing agent, Sylgard 184, Dow Corning) was cured on silicon wafers patterned with SU-8 features, and devices were bonded to PDMS-coated glass slides. Prepolymer solutions were prepared by mixing 20% (v/v) poly (ethylene glycol) diacrylate (PEGDA;  $M_n = 700$ , Sigma-Aldrich), 5% 2-hydroxy-2-methyl-propiofenone (photoinitiator, Sigma-Aldrich), 25% DI water, and 50% polyethylene glycol (PEG;  $M_n = 200$ , Sigma-Aldrich).

Using the previously reported SFL setup<sup>49,50</sup>, prepolymer solution was loaded into the synthesis device by pressure-controlled flow. After stopping the flow, particles were polymerized by ultraviolet light (Thorlabs, 365 nm LED, 2200  $\text{mW cm}^{-2}$ ) in mask-defined shapes (transparency masks designed in AutoCAD, printed by Fineline Imaging). The three steps (flow, stop, exposure) were repeated to achieve semi-continuous particle synthesis. Polymerized particles were collected from the channel outlet and purified with PBST (phosphate buffered saline with 0.05% Tween-20) by centrifugation. Hydrogel microparticles with varying elastic modulus (Fig. 1g) were synthesized using the SFL setup. Prepolymer solutions were prepared with varying concentrations of PEGDA ( $M_n = 700$ ) in the range 10-35% (v/v), plus 5% photoinitiator, 25% DI water, and PEG ( $M_n = 200$ ) in the range 35-60% to make up the remaining volume. For all prepolymer compositions, particles were polymerized using an 11  $\mu\text{m}$  circle mask in microfluidic channels with heights of 10  $\mu\text{m}$ , resulting in a particle heights of 7-8  $\mu\text{m}$ .

Hydrogels of three aspect ratios 1.0, 1.5 and 2.5 (Supplementary Fig. 3) were fabricated by using three masks with same cross-sectional area for exposure, but three different shapes, respectively: a 11 $\mu\text{m}$ -diameter circle, an ellipse with aspect ratio 1.5 (major axis: minor axis), and an ellipse with aspect ratio of 2.5. The volumes of hydrogels were measured using the Dynamic Light Scattering (DLS) with means 655, 658 and 602  $\mu\text{m}^3$  for aspect ratios 1, 1.5 and 2.5, respectively. Particle dimensions (height and major/minor axes) were measured from brightfield microscopy images using ImageJ software, taking an average from at least ten particles.



### **Measurement of particle elastic modulus by atomic force microscopy (AFM)**

To determine the elastic modulus of the hydrogel microparticles, force spectroscopy measurements were performed using a MFP-3D-BIO atomic force microscope with an integrated optical microscope (Asylum Research). A 50  $\mu\text{L}$  drop of particle solution ( $\sim 10$  particles in PBST) was placed on a glass slide. Silicon nitride cantilevers with silica spherical indenters of 10  $\mu\text{m}$  diameter (Novascan) were used to indent the particles in PBST after they settled to the surface of the slide. For particles with composition 10-25% PEGDA, a cantilever with nominal spring constant of 0.12  $\text{N m}^{-1}$  was used. For stiffer particles with higher composition 30-35% PEGDA, a cantilever with nominal spring constant 0.35  $\text{N m}^{-1}$  was used. The inverse optical lever sensitivity (InvOLS) for each cantilever was calibrated from deflection-displacement curves on a rigid glass slide (23.21 and 17.46  $\text{nm V}^{-1}$ , respectively) and the actual spring constant of each cantilever was measured using the thermal noise method<sup>51</sup> to be 0.114 and 0.475  $\text{N m}^{-1}$  respectively. For each sample, we indented four particles with four indents per particle. Elastic modulus was calculated by fitting the force-indentation curves to a maximum indentation depth of 400 nm using the Hertz model for spherical elastic contact with IGOR data processing software (Wavemetrics). The indentation velocity was 1  $\mu\text{m s}^{-1}$ . The PEGDA hydrogels were assumed to be incompressible elastic materials, with a Poisson's ratio of 0.5<sup>52,53</sup>.

### **Cell culture, chemical perturbations and transfections**

L1210 and BaF3 cells were cultured in RPMI containing L-glutamine, Phenol Red, 11 mM D-glucose, and the RPMI was supplemented with 10% heat inactivated fetal bovine serum (FBS), 10mM HEPES, 100 units/mL of penicillin, 100  $\mu\text{g/mL}$  of streptomycin, and 0.25  $\mu\text{g/mL}$  of Amphotericin B. S-HeLa cells were cultured in DMEM containing L-glutamine, Phenol Red, 25 mM D-glucose, and the DMEM was supplemented as RPMI. All cell culture reagents were obtained from Thermo Fisher Scientific, except FBS which was obtained from Sigma-Aldrich. The L1210 cells were obtained from ATCC (CCL-219). BaF3 cells expressing BCR-ABL were obtained from RIKEN BioResource center. S-HeLa cells were a gracious gift from Dr. Kevin Elias (Brigham and Women's Hospital). All experiments were started from cell cultures that had not reached more than 40% confluence.

For chemical perturbations, cells were pretreated with chemicals for 20-30 min under normal cell culture conditions and loaded into the SMR along with the chemical containing media. Chemical concentrations used were 0.1% DMSO (controls, Sigma-Aldrich), 0.02 – 1  $\mu\text{M}$  Latrunculin B (Sigma-Aldrich), 1  $\mu\text{M}$  Cytochalasin D (Sigma-Aldrich), 25  $\mu\text{M}$  (inhibiting Cytokinesis, long-term traces) or 50  $\mu\text{M}$  (Actomyosin cortex disruption, end-point assay) Blebbistatin (Sigma-Aldrich), 10  $\mu\text{M}$  EIPA (Sigma-Aldrich), 5  $\mu\text{M}$  STLC (Sigma-Aldrich) and 2  $\mu\text{M}$  RO3306 (R&D Systems). For surface crosslinking experiment, cells were treated with 4% PFA (Electron Microscopy Sciences) in PBS for 1 or 10 min. Cells were then washed with PBS and resuspended in normal culture media. For all wash and re-suspension steps, cells were centrifuged at 500 g for 2 min. For the osmotic challenge, desired osmolarity of the external solutions were achieved by mixing cell culture media with deionized water or D-mannitol (Sigma-Aldrich) for hypotonic or hypertonic conditions, respectively. Cell culture media was set to be isotonic (300 mOsm). Cells in the culture media were mixed 1:1 with the prepared external solution (e.g. mixed 1:1 with 500 mOsm solution to achieve final osmolarity of 400 mOsm) to obtain desired osmolarity. We kept the cells in the prepared media solution at room temperature for 20 min before loading them into the SMR containing media of the desired osmolarity. For hypotonic experiment shown in Fig. 4d, cells were loaded immediately after the osmotic shock. For the slow hypotonic shock condition shown in Supplementary Fig. 11, cells were treated with DI water every 2 minutes for a total of 20 minutes. The desired osmolarity of 250 mOsm was achieved by adding 10 $\mu\text{L}$  of water every 2 min (total of 10 times) into 500  $\mu\text{L}$  of cell solution.

L1210 FUCCI cells, which express the fluorescence cell cycle marker construct mAG-hGem, were generated in a previous study<sup>34</sup>. These cells were transfected with LifeAct, a F-actin labelling red fluorescent protein construct<sup>31</sup>, using rLVUbi-LifeAct-TagRFP lentiviral vector obtained from ibidi

GmbH. Several rounds of transfections were carried out using spinoculation. In short,  $1.5 \times 10^5$  L1210 FUCCI cells were mixed with 10  $\mu\text{g/ml}$  Polybrene (EMD Millipore) and  $1 \times 10^6$  TU of lentivirus, and the mixture was centrifuged at 800 g for 60 min at 25°C. After centrifugation, the cells were moved to normal cell culture media, grown overnight and the spinoculation procedure was repeated. After 3 rounds of transfections cells were moved to normal culture media and 24 h later selection was started by adding 10  $\mu\text{g/ml}$  Puromycin (Sigma-Aldrich). After a week of selection, the transfected population was enriched for cells expressing high levels of LifeAct by FACS sorting using BD FACS Aria.

### Size normalizing node deviation to obtain SNACS values

Since node deviation decreases with particle volume (Fig. 1f, Fig. 2b), size-normalization is required to compare node deviation of different size particles or cells. To obtain the size-normalized acoustic scattering (SNACS), we first obtained the volume following a previously described method<sup>5</sup>. In short, we converted buoyant mass obtained from individual peaks (Supplementary Fig. 4a) to volume using a median density of the population. Median density of the population relative to the fluid ( $\bar{\rho} = \bar{\rho}_c - \rho_f$ ) was obtained by fitting buoyant mass distribution with a log-normal distribution to estimate the mean buoyant mass ( $\bar{BM}$ ,  $> 300$  cells). Mean volume ( $\bar{V}$ ) was obtained by fitting the log-normal distribution to the volume distribution obtained from the Coulter Counter measurements (Beckman Coulter, 5000 counts). Single-cell volume was then obtained using the following equation:

$$V = BM / \bar{\rho}, \text{ where } \bar{\rho} = \frac{\bar{BM}}{\bar{V}}$$

The mean density ( $\bar{\rho}$ ) of the population was calculated for each condition. Then, the node deviation for each cell (Supplementary Fig. 4a) was divided by its volume ( $V$ ) to obtain node deviation/volume ( $NV$ ). Representing each cell as a data point in the scatter plot ( $NV$  vs  $V$ , Supplementary Fig. 4b), an iso-elasticity line of slope  $m$  is passed through each point (Supplementary Fig. 4c). All data points along a given iso-elasticity line have the same mechanical property based on the FEM simulation (Fig. 2b). Finally, the SNACS for each cell was obtained by taking the linear interpolation of  $NV$  at  $V_{ref}$  along the iso-elasticity line (Supplementary Fig. 4d):

$$\text{SNACS} = NV - m(V_{ref} - V)$$

The slope ( $m$ ) was obtained by performing a linear regression on the population data (typically  $> 300$  cells) in the  $NV$  versus  $V$  scatter plot (Fig. 2b). The reference volume ( $V_{ref}$ ) was set to the median volume of the population, which for L1210 cells was 900 fL.

### Cell cycle transition points

To pinpoint the G2/M transition, we utilized a previously reported finding that mitotic swelling starts in early prophase and prometaphase<sup>36</sup>. As the SNACS decrease was simultaneous with swelling (Fig. 4a), and SNACS decrease was not observed in G2 arrested cells (Supplementary Fig. 10a), we marked the G2/prophase transition to take place right before the SNACS decrease starts. The FUCCI signal (mAG-hGem) decrease (when fluorescence first reaches 85% of the maximum value) was used to mark the metaphase to anaphase transition. Based on fluorescence imaging, we obtained the average time lag between the time when FUCCI signal (mAG-hGem) begins to drop (below 85% maximum) and the first time point for when a cell deviates from spherical to be approximately 3.8 min. Then, to assign the cell cycle transition points in figures, we subtracted the 3.8 min time lag from the first time point when cell shape deviates from sphere to mark the start of anaphase. SNACS traces of the metaphase arrested cells (treated with STLIC), where SNACS remained low for several hours, supported our timing of the metaphase-anaphase transition (Fig. 4b).

### Microscopy

L1210 cells expressing the FUCCI (mAG-hGem) and LifeAct-RFP F-actin probe (rLVUbi-LifeAct-TagRFP) constructs were imaged on poly-lysine coated glass bottom CellView cell culture dishes

(Greiner Bio-One). Media, CO<sub>2</sub> and temperature conditions during the imaging were the same as within the SMR. Imaging was carried out using DeltaVision widefield deconvolution microscope with standard FITC and TRICT filters, 100X oil immersion objective and immersion oil with refractive index of 1.522. No binning was used and the image resolution was 9.245 pixels/ $\mu\text{m}$  in xy-planes. When examining the effects of actin perturbing chemicals on the F-actin structure, a 3  $\mu\text{m}$  thick section from the middle of the cells was imaged in 0.2  $\mu\text{m}$  thick z-layers. After the first round of imaging, the cells were treated with the indicated chemical for 30 min and the same cells were imaged again. When examining the F-actin distribution in early mitosis, a 1  $\mu\text{m}$  thick section from the middle of the cells was imaged in 0.2  $\mu\text{m}$  thick z-layers every 5 min. Only the middle z-layer was used for final analysis and presentation. When examining the F-actin distribution during cytokinesis, three 0.2  $\mu\text{m}$  thick z-layers were imaged with 1  $\mu\text{m}$  height intervals to capture both the mother and the daughter cells at the central height of the cell, and this imaging was repeated every 2.5 min. The total duration of all imaging experiments was limited to 5 h, as prolonged light exposure induced phototoxicity and started to interfere with mitotic progression.

### **Image analysis – actin cortex thickness in early mitosis**

All images were deconvolved using standard settings in the softWoRX software. To normalize the effect of photo-bleaching, first we calculated the total LifeAct signal in the entire images (2048 x 2048 pixels) that contained multiple cells. Then, we fitted a second order polynomial to the total LifeAct signal in the image as a function of frame index. During the subsequent image analyses, we corrected the LifeAct intensity with the corresponding decay coefficient calculated from the polynomial fit for each frame. To analyze individual cells, we first determined the representative cells that went through the nuclear envelope breakdown and/or cytokinesis during the experiment. These cells were cut out of the larger images and analyzed individually (Supplementary Fig. 12a).

For analyzing each cell, we utilized MATLAB's circular Hough transform algorithm to detect circles on images (*imfindcircles*). We applied this algorithm to binary images that were processed by a 2-dimensional median filter with 3-by-3 neighborhood (Supplementary Fig. 12b) and a threshold filter (Supplementary Fig. 12c). After determining an initial position for the cell center and radius (Supplementary Fig. 12d) we obtained the actin signal at the raw, unfiltered image across 100 radial paths around the detected circle ranging from the estimated cell center to 125% of the estimated cell radius (Supplementary Fig. 12e). Then, we recorded the prominent peak location of the actin signal that was closest to the estimated radius as the cortex position for that particular radial path. We took the median of LifeAct signals recorded from each radial path after aligning them at their calculated cortex locations (Supplementary Fig. 12f). Using this median LifeAct profile of the cell cross-section, we calculated the full width at half maximum (FWHM) of the LifeAct signal at the cortex (Supplementary Fig. 12f, red circles) in reference to the LifeAct signal that is recorded at the cytoplasm. We defined the baseline signal at the cytoplasm of L1210 cells as approximately 85 to 90% of the radial measurement path (Supplementary Fig. 12f, red line). This FWHM value of LifeAct at the cortex functioned as a proxy for the cortex thickness.

To analyze F-actin distribution dynamics through mitosis, we repeated our analysis for each time point we collected throughout the experiment. At each time point we also analyzed the distribution of the FUCCI signal (mAG-hGem) in the cell (Supplementary Fig. 12g). We aligned the data from different cells to the time of nuclear envelope breakdown using the FUCCI signal (mAG-hGem) spread from nucleus to across the entire cell area as marker for the nuclear envelope breakdown (Supplementary Fig. 12h). Finally, for comparing different cells, we normalized the FWHM signals of each cell with respect to the median FWHM signal that was recorded from the frames of that cell prior to the nuclear envelope breakdown.

### **Image analysis – equatorial and polar actin cortex density during mitosis**

To study how the distribution of F-actin changes through mitosis, we considered four regions of the cell. Each region covers a 90-degree area extending from 65% of the estimated radius of the cell to its full radius. We utilized the same cell detection algorithm that was described in the previous section, with the additional capability of detecting two adjacent cells (Supplementary Fig. 12i,j). To determine the division axis and the regions of interest we started the analysis from the frames after cytokinesis with two cells clearly visible, and worked back in time until the onset of anaphase. At each time point, if we detected two cells, even if the cell was in mid-anaphase, we determined the division axis and the equatorial and polar regions of interest. We set the polar region as the 90-degree segments that are at two opposite sides of the detected cells (Supplementary Fig. 12k). We set the equatorial region as the regions that are in the middle of the two cells and have an angular span that is perpendicular to the polar regions (Supplementary Fig. 12l). To compensate for the observed non-circular shapes, we utilized an edge detection algorithm to determine the true extent of the cells overlapping with the region of interest. If we detected a single cell, we defined the four equal area regions using the same angular span that was determined in the previous frames (during cytokinesis) of the same cell. Finally, we calculated the relative F-actin density in each region by normalizing the total LifeAct signal to the area in each region. In the cases, where an adjacent, brighter cell was interfering with the cell of interest, we disregarded the signal in the affected region. Finally, we aligned the timing of different cells using the first frame, where two separate cells are apparent (mid-anaphase).

### Data presentation

To characterize the system noise, we repeatedly measured node deviation of the same 12  $\mu\text{m}$  diameter polystyrene bead, size-normalized to SNACS and calculated their standard deviation (Supplementary Fig. 6a). SNACS of L1210 cells ( $n = 24$  cells) were aligned to the latest time point where the cells maintained round morphology (3.8 min after anaphase onset, Fig. 3c,d). Then, we interpolated each data points for 0.01 h and calculated the mean value and standard deviation out of the interpolated data for each time point. All SNACS plots were filtered with median filter of length 3, except in late mitosis (data points after anaphase onset) where we show raw data. From the onset of anaphase, we calculated P values between the maximum and minimum within moving 5 minute time block to characterize how much of the temporal change has statistical significance. We observed that temporal SNACS changes were not significant ( $P > 0.05$ , two-sided Welch's t-test) from 15.2 min after the onset of anaphase to cell division (Fig. 3, red dashed lines).

After defining the size-normalized acoustic scattering parameter SNACS at the end of Fig. 2, we illustrated all node deviation changes, which reflect the mechanical property of a cell, using SNACS or  $\Delta\text{SNACS}$ .  $\Delta\text{SNACS}$  represents the change in SNACS relative to the median value of first 10-15 minutes of data presented (except in Fig. 4d, where mean value of the whole cells before hypotonic shock is used), and is only used for better visualization of data.

### Statistics and Reproducibility

To quantify the agreement between the data from the experiments and the simulations (Fig. 1d-f), we calculated the coefficient of determination R-squared ( $R^2$ ). We assumed that the observed data are the experiments and the fitted are the simulations. Thus, for number N of data points where  $y_{i,\text{experiment}}$  and  $y_{i,\text{simulation}}$  are the observed and the fitted values ( $i=1,2,\dots,N$ ), we calculated:

$$R^2 = 1 - \frac{\sum (y_{i,\text{experiment}} - y_{i,\text{simulation}})^2}{\sum (y_{i,\text{experiment}} - \bar{y})^2}, \text{ where } \bar{y} = \frac{1}{N} \sum y_{i,\text{experiment}}$$

Statistical analysis were performed by Origin and MATLAB. We performed two-sided Welch's t-test for comparisons between two groups and one-way ANOVA for comparisons between multiple groups. Post hoc analysis (Fisher's LSD) was performed only when ANOVA yielded a statistical difference ( $P < 0.05$ ). Null hypothesis was always that mean values are the same. The detailed statistics performed for each experiment are shown in figure legends.

All single-cell SNACS traces were obtained on separate days. All single-cell SNACS traces were repeated at least five times in independent experiments. The population SNACS measurements were repeated at least in three independent experiments, yielding comparable results.

**FEM simulation**

See Supplementary Note 2 for details.

**Mass distribution correction**

See Supplementary Note 3 and Supplementary Fig. 9 for details.

**Orientation-dependent noise**

See Supplementary Note 4 and Supplementary Fig. 15 for details.

**Cortical thickness reduction during swelling**

See Supplementary Note 5 for details.

**Reporting Summary**

Further information on research design is available in the Life Sciences Reporting Summary.

## Data availability

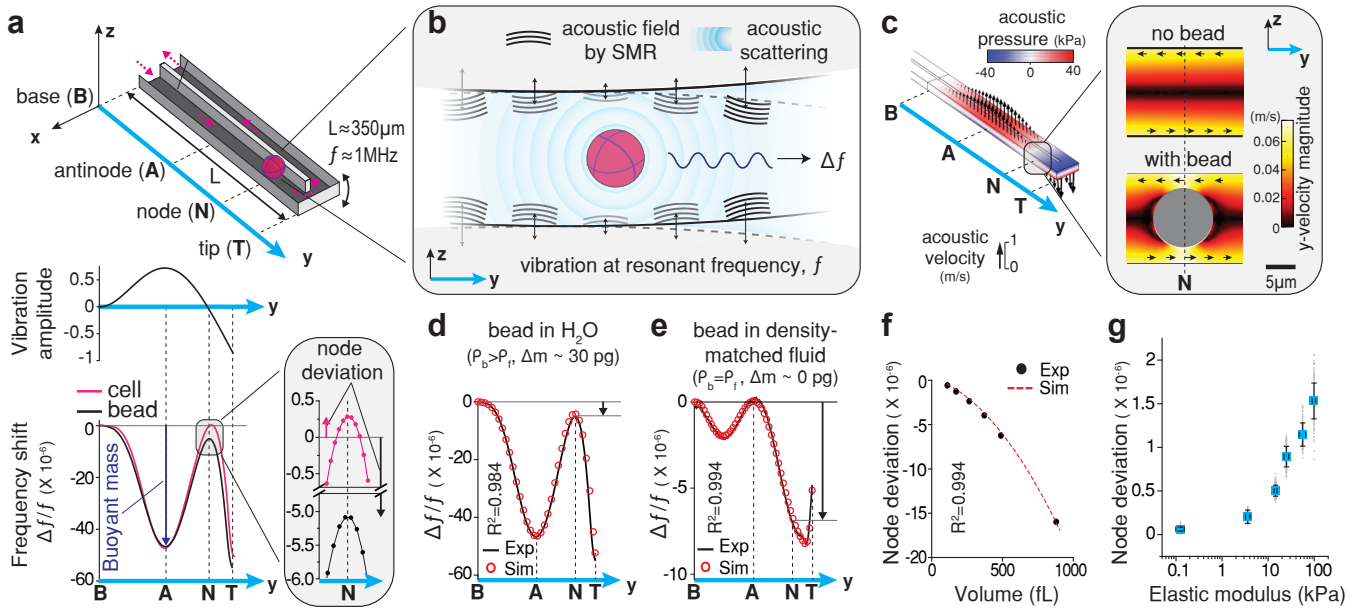
The data that support the findings of this study are available from the corresponding author on reasonable request.

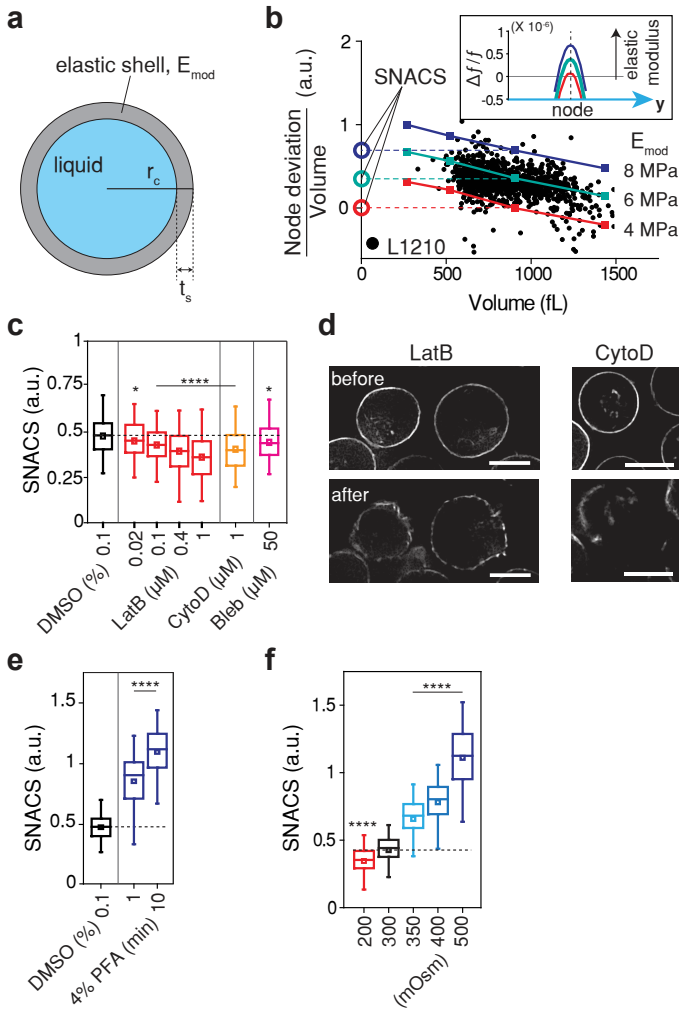
## Code availability

Code used in this study can be obtained from the corresponding author upon reasonable request.

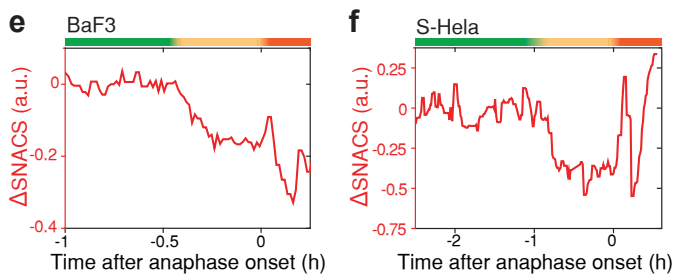
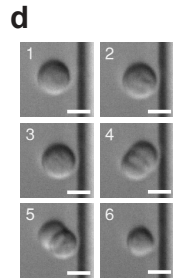
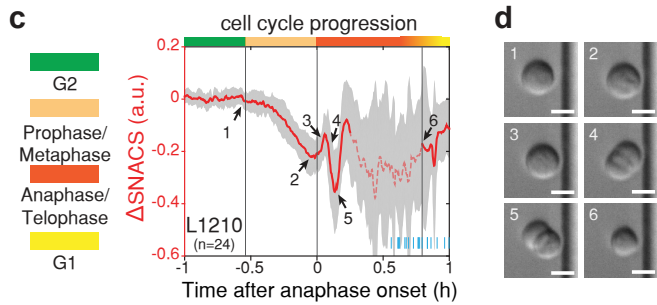
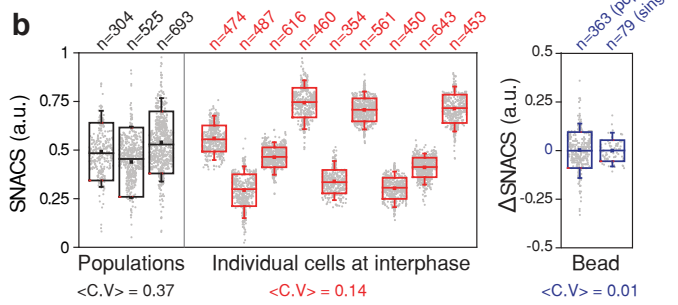
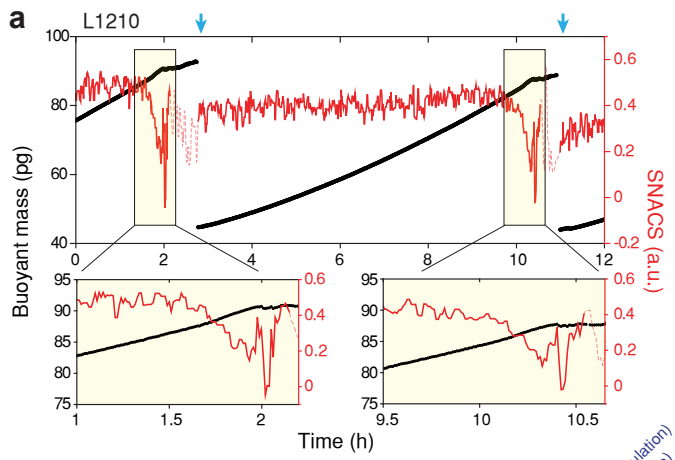
## Methods-only references

- 46 Lee, J. *et al.* Suspended microchannel resonators with piezoresistive sensors. *Lab Chip* **11**, 645-651 (2011).
- 47 Cetin, A. E. *et al.* Determining therapeutic susceptibility in multiple myeloma by single-cell mass accumulation. *Nat Commun* **8**, 1613 (2017).
- 48 Olcum, S., Cermak, N., Wasserman, S. C. & Manalis, S. R. High-speed multiple-mode mass-sensing resolves dynamic nanoscale mass distributions. *Nat Commun* **6**, 7070 (2015).
- 49 Dendukuri, D., Pregibon, D. C., Collins, J., Hatton, T. A. & Doyle, P. S. Continuous-flow lithography for high-throughput microparticle synthesis. *Nat Mater* **5**, 365-369 (2006).
- 50 Dendukuri, D., Gu, S. S., Pregibon, D. C., Hatton, T. A. & Doyle, P. S. Stop-flow lithography in a microfluidic device. *Lab Chip* **7**, 818-828 (2007).
- 51 Hutter, J. L. & Bechhoefer, J. Calibration of Atomic-Force Microscope Tips (Vol 64, Pg 1868, 1993). *Review of Scientific Instruments* **64**, 3342-3342 (1993).
- 52 Elbert, D. L. & Hubbell, J. A. Conjugate addition reactions combined with free-radical cross-linking for the design of materials for tissue engineering. *Biomacromolecules* **2**, 430-441 (2001).
- 53 Anseth, K. S., Bowman, C. N. & BrannonPeppas, L. Mechanical properties of hydrogels and their experimental determination. *Biomaterials* **17**, 1647-1657 (1996).

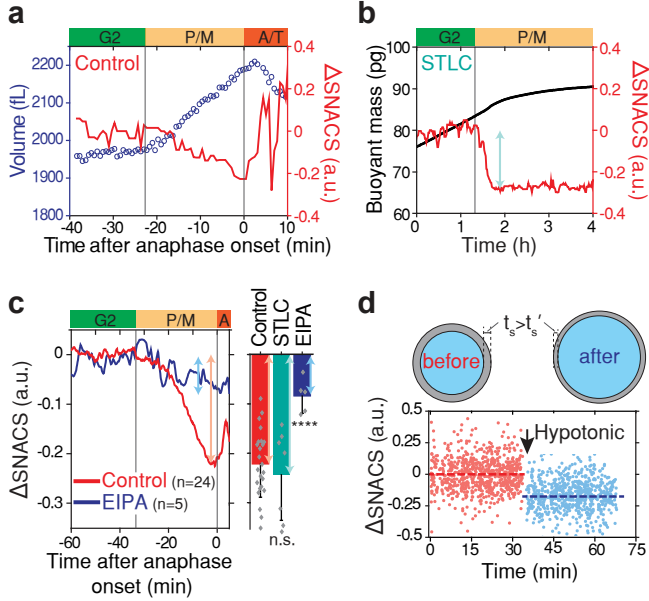




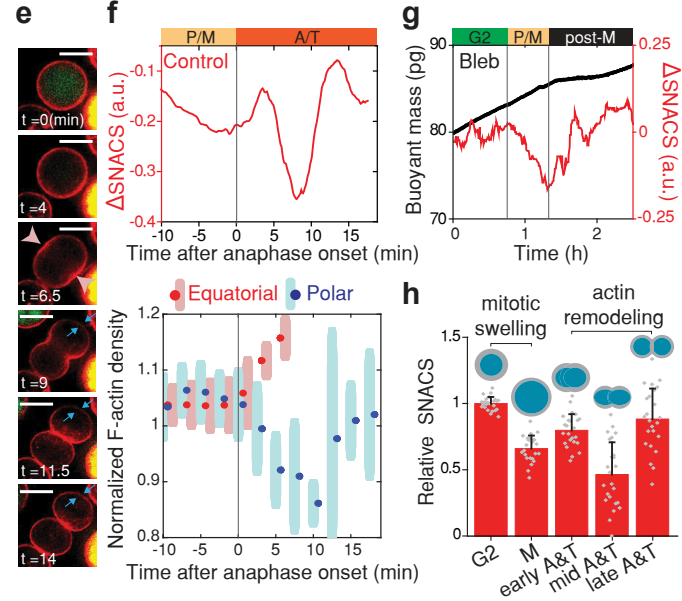




### Early mitosis



### Late mitosis & summary



**Supplementary Table 1****List of energy terms.**

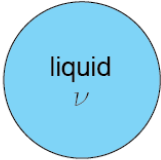
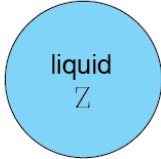
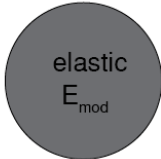
Parameter	Equation	Description
$U_f$	$\int_f \left[ \frac{p_1^2}{2\rho c^2} \right] dV$	acoustic potential energy
$T_f$	$\int_f \left[ \frac{1}{2} \rho v_1^2 \right] dV$	acoustic kinetic energy
$U_{p,s}$	$\int_{p,s} \left[ \frac{1}{2} \sigma_{ij} \epsilon_{ij} \right]$	particle (shell) potential energy (elastic deformation)
$T_{p,s}$	$\int_{p,s} \left[ \frac{1}{2} \rho x^2 \omega^2 \right]$	particle (shell) kinetic energy
$U_c$	$\int_c \left[ \frac{p_1^2}{2\rho c^2} \right] dV$	liquid core acoustic potential energy (only applies to the cell model)
$T_c$	$\int_c \left[ \frac{1}{2} \rho v_1^2 \right] dV$	liquid core acoustic kinetic energy (only applies to the cell model)

**Supplementary Table 2****List of simulation parameters.**

Parameter	Values (units)	Description
$w$	20 ( $\mu\text{m}$ )	buried channel width
$h$	15 ( $\mu\text{m}$ )	buried channel height
$L$	315, 350 ( $\mu\text{m}$ )	cantilever (channel) length
$t$	2 ( $\mu\text{m}$ )	top, bottom silicon layer thickness
$d$	5 ( $\mu\text{m}$ )	fluid channel separation
$A$	1-100 ( $\mu\text{m}$ )	vibration amplitude
$r_p$	3 - 6 ( $\mu\text{m}$ )	particle radius
$r_c$	3 - 7 ( $\mu\text{m}$ )	total radius of a cell model
$t_s$	0.5 - 5(%)	thickness of the shell, relative to the radius
$E_p$	0.1 - 100 (MPa)	bulk Young's modulus of the particle
$E_s$	2-10 (MPa)	Young's modulus of the shell in liquid-core elastic-shell model
$\rho_f$	0.997 - 1.08 ( $\text{g}/\text{cm}^3$ )	fluid density
$\rho_c$	1.05 ( $\text{g}/\text{cm}^3$ )	cell density (both inner core and outer shell)
$\rho_p$	1.05 ( $\text{g}/\text{cm}^3$ )	bead density
$\nu_c$	0.5	cell poisson's ratio (outer shell)
$\nu_p$	0.34	bead poisson's ratio

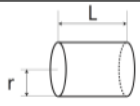

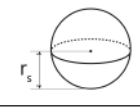
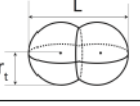
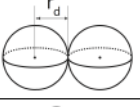
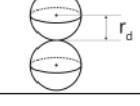
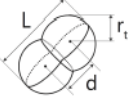
**Supplementary Table 3**

**Different mechanical models.**

Model	Model illustration	Simulation result
Viscous drop		cannot reproduce positive node deviation
Acoustic Impedance Mismatch		cannot reproduce positive node deviation
Bulk Elastic		can reproduce positive node deviation, but results in positive slope of isoelasticity line

**Supplementary Table 4**

**Mass distribution function ( $\lambda(x)$ ) for selected geometries and orientations.**

Geometry	$\lambda(x)$	integration interval	Description (used)
	$\pi r^2$	$\left[-\frac{L}{2}, \frac{L}{2}\right]$	cylinder parallel (hydrogels)
	$2L\sqrt{r^2 - x^2}$	$[-r, r]$	cylinder perpendicular (hydrogels)
	$\pi(r_s^2 - x^2)$	$[-r_s, r_s]$	sphere (before anaphase)
	$\begin{cases} \pi(r_t^2 - (x + d/2)^2), & x < 0 \\ \pi(r_t^2 - (x - d/2)^2), & x > 0 \end{cases}$	$\left[-\frac{L}{2}, \frac{L}{2}\right]$	overlapping spheres (during anaphase transition)
	$\begin{cases} \pi(r_d^2 - (x + r_d)^2), & \text{if } x < 0 \\ \pi(r_d^2 - (x - r_d)^2), & \text{if } x > 0 \end{cases}$	$[-2r_d, 2r_d]$	doublet parallel (after anaphase transition)
	$2\pi(r_d^2 - x^2)$	$[-r_d, r_d]$	doublet perpendicular (after anaphase transition)
	$\begin{cases} \pi r_1^2, & \text{if } x < -q \\ \pi r_2^2, & \text{if } x > q \\ A(r_1, r_2, d/2 \sin \theta), & \text{else} \end{cases}$	$\left[-\frac{L}{2} \cos \theta, \frac{L}{2} \cos \theta\right]$	overlapping spheres rotated (during anaphase transition)

Note:  $r_1 = \sqrt{r_t^2 - (x + q)^2}$ ,  $r_2 = \sqrt{r_t^2 - (x - q)^2}$ ,  $q = d/2 \cos \theta$

$A(r_1, r_2, d)$  refers to the area of overlapping circles of radius  $r_1$  and  $r_2$ , with their center separated by a distance of  $d$

**Supplementary Table 5****List of calculated cortical thickness change upon isometric volume expansion.**

swelling amount (% volume)	absolute cortex thickness change (%)	cortex thickness to diameter after swelling (%)	Note
0	0	1	
10	6.33	0.907	
14.1	8.65	0.874	plotted in Fig. 4d
15	9.14	0.867	
20	11.75	0.831	

## Supplementary Note 1. Theory

### 1.1 Introduction

Using the Rayleigh Ritz Theorem, which equates time average kinetic energy and time averaged potential energy, resonant frequency of the Suspended microchannel resonator (SMR) containing a particle immersed in the fluidic channel can be obtained<sup>1</sup>. It has been shown previously that a point-mass particle in the SMR of length  $L$  vibrating at its second mode shifts the resonant frequency as a function of particle position ( $y$ ) along the cantilever<sup>2</sup>,

$$\left(\frac{\Delta f_2}{f_2}\right) = -1 + \left[1 + u_2^2(y/L) \frac{\Delta m}{m_{eff}}\right]^{-1/2} \approx -\frac{1}{2} u_2^2(y/L) \frac{\Delta m}{m_{eff}} \quad (1)$$
$$u_2(x) = \frac{1}{2} \left[ (\cosh(\lambda_2 x) - \cos(\lambda_2 x)) - \left( \frac{\cosh(\lambda_2) + \cos(\lambda_2)}{\sinh(\lambda_2) + \sin(\lambda_2)} \right) (\sinh(\lambda_2 x) - \sin(\lambda_2 x)) \right]$$

where  $f$  is the resonant frequency of SMR vibrating at its second mode before the particle is introduced,  $u_2$  is the normalized second mode shape,  $\Delta m$  is the mass change in the system upon loading the particle,  $m_{eff}$  is the effective mass of the unloaded cantilever, and  $\lambda_2$  is the eigenvalue for the second mode ( $\lambda_2 = 4.6941$ ). According to Eq. (1), the resonant frequency does not change when a particle is at the node (i.e.,  $\Delta f/f|_{node} = 0$  when  $u_2(y) = 0$ ). However, we observe a non-zero frequency shift at the node (i.e. node deviation) from beads and cells (Fig. 1a).

In this note, we start our discussion with the theory that was developed to derive Eq. (1) and provide the assumptions that led to a discrepancy between theory (according to Eq. (1)) and measured node deviation (Fig. 1a). Next, we provide the details of the FEM simulation, which revealed new energy terms that were accounted for when calculating the resonant frequency change. Finally, we derive a new expression for the frequency response based on the FEM simulation results that successfully described node deviation measurements for both beads and cells (Figs. 1d,e and 2b).

### 1.2 Theory

We assume the vibration amplitude of the SMR follows the normalized second mode shape ( $u_2$ ) from Euler-Bernoulli beam equation and is unchanged for sufficiently small mass loading ( $\Delta m \ll m_{eff}$ )<sup>1</sup>

$$z(y, t) = Au_2\left(\frac{y}{L}\right) \cos(\omega t) \quad (2)$$
$$= Au(y) \cos(\omega t)$$

where  $A$  is the maximal amplitude and  $\omega = 2\pi f$  for a SMR vibrating harmonically with frequency  $f$ . For this note,  $u(y)$  refers to the normalized second mode shape. In the earlier theory, potential energy from the bending of the silicon layer surrounding the fluidic channel (Supplementary Fig. 1a) was considered to be the only term contributing to the total potential energy of the system,  $U_{total}$ . Therefore,

$$U_{total}(t) = U_{sil}(y, t)$$
$$= \int_0^l \frac{1}{2} EI \left( \frac{\partial z}{\partial y} \right)^2 dy$$
$$= \left[ A^2 \int_0^l \frac{1}{2} EI \left( \frac{\partial u}{\partial y} \right)^2 dy \right] \cos^2(\omega t) \quad (3)$$
$$= U_{max} \cos^2(\omega t)$$



For the kinetic energy of the system,  $T_{total}$ , there are three contributing sources for kinetic energy (silicon layer, fluid, and particle) for which we provide

$$\begin{aligned}
T_{total}(y, t) &= T_{sil}(y, t) + T_f(y, t) + T_p(y, t) \\
&= \int_{sil} \frac{1}{2} \rho_{sil} \left( \frac{\partial z}{\partial t} \right)^2 dV + \int_f \frac{1}{2} \rho_f \left( \frac{\partial z}{\partial t} \right)^2 dV + \frac{1}{2} m_p \left( \frac{\partial z}{\partial t} \right)^2 \\
&= A^2 \left[ \int_{sil} \frac{1}{2} \rho_{sil} \omega^2 u^2 dV + \int_f \frac{1}{2} \rho_f \omega^2 u^2 dV + \frac{1}{2} m_p \omega^2 u^2(y) \right] \sin^2(\omega t)
\end{aligned} \tag{4}$$

where  $m_p$  is the mass of the particle,  $\rho_{sil}$  and  $\rho_f$  are the densities of silicon layer and fluid, respectively. In the existing theory, the interaction between the fluid and particle is ignored and it is assumed that the particle and fluid have the same kinetics (i.e.,  $v(y) = \omega u(y)$ ). For this case, Eq. (4) simplifies to

$$\begin{aligned}
T_{total}(y, t) &= \frac{1}{2} A^2 \omega^2 [m_{eff} + (m_p - m_f) u^2(y)] \sin^2(\omega t) \\
&= T_{max}(y) \sin^2(\omega t)
\end{aligned} \tag{5}$$

where  $m_{eff} = \frac{1}{2} \int \rho u^2 dV + \frac{1}{2} \int \rho_f u^2 dV$  when  $y = 0$ . Thus, using the Rayleigh-Ritz Theorem to equate the time-averaged potential energy  $U_{max}/2$  with the time-averaged kinetic energy  $T_{max}/2$  at  $y=0$

$$U_{max} = T_{max} = \frac{1}{2} A^2 \omega_0^2 m_{eff} \tag{6}$$

where we set  $\omega = \omega_0$  when  $y=0$  (i.e., resonant frequency before particle enters the channel). We assume the potential energy of a system is not affected by the particle position and therefore constant ( $U_{max} = C$ ). Then, applying Rayleigh-Ritz Theorem to equate  $U_{max}/2$  and  $T_{max}/2$  at non-zero and using Eq. (5),

$$\frac{1}{2} A^2 \omega_0^2 = \frac{1}{2} A^2 (\omega_0 + \Delta\omega)^2 (m_{eff} + \Delta m u^2(y)) \tag{7}$$

where  $\Delta m = m_p - m_f$  and  $\omega = \omega_0 + \Delta\omega$ . This then simplifies to Eq. (1),

$$\left( 1 + \frac{\Delta\omega}{\omega_0} \right)^{-2} = 1 + u^2(y) \frac{\Delta m}{m_{eff}} \tag{8}$$

So far, we have described how energy balance between kinetic and potential energy of the system collectively changes the resonant frequency of SMR. However, acoustic features in the SMR were ignored and several energy terms associated with acoustic fields in the SMR were neglected. First, we have assumed that the only term contributing to the potential energy is from the silicon layer. However, the potential energy stored in acoustic standing waves (Supplementary Fig. 1b and Supplementary Video 1) in the embedded microfluidic channel, as well as the energy stored in the elastic materials (particle and shell of the cell model) should also be included. Second, we have only considered velocities in the z-direction (i.e., normal to the surface of the cantilever, Supplementary Fig. 1c). We determined that the velocities along the cantilever (y-direction) could be as large as 10% that of the z-direction (Supplementary Fig. 1c, inset), and in the immediate vicinity of the node, the velocity in the y-direction is even greater than in the z-direction. Third, and most importantly, we have neglected the interaction between the particle and fluid environment by assuming the particle and nearby fluid have the same kinetics. However, as the particle scatters the acoustic field, it alters the kinetics of the neighboring fluid medium as well (Fig. 1c, inset and

Supplementary Video 2). By incorporating these three considerations into our FEM model, our simulation results match the experimental results (Fig. 1d,e and Supplementary Fig. 2).

### 1.3 Acoustofluidics

To develop a more general theory that includes the effect of the acoustic field, we begin with the governing equations for the fluids and their acoustic energies. Kinetics of a fluid is determined by its density  $\rho$ , pressure  $p$ , and individual fluid particle velocity  $v$ . These parameters are governed by the continuity equation for the mass and the Navier-Stokes equation<sup>3</sup>. Acoustic fields that result from a perturbation to these parameters can be written in terms of the zeroth, first, second, and third and higher-order terms as

$$\begin{aligned}\rho &= \rho_0 + \rho_1 + \rho_2 + \dots \\ p &= p_0 + p_1 + p_2 + \dots \\ \vec{v} &= \vec{v}_0 + \vec{v}_1 + \vec{v}_2 + \dots\end{aligned}\tag{9}$$

where the subscripts denotes the order of perturbation. 0<sup>th</sup> order represents the quiescent state and for simplicity we take  $v_0 = 0$ .

Taking only the 1<sup>st</sup> order perturbations into account and neglecting 2<sup>nd</sup> and higher order terms, the governing equations for fluids can be simplified into a wave equation

$$\nabla^2 p_1 = \frac{1}{c_0^2} \frac{\partial^2 p_1}{\partial t^2}\tag{10}$$

where  $c_0$  is the speed of sound in the fluid, and  $p_1 = c_0^2 \rho_1$ . Assuming time-harmonic fields,

$$\begin{aligned}\rho_1(\vec{r}, t) &= \Re \{ \tilde{\rho}_1(\vec{r}) e^{-i\omega t} \} \\ p_1(\vec{r}, t) &= \Re \{ \tilde{p}_1(\vec{r}) e^{-i\omega t} \} \\ \vec{v}_1(\vec{r}, t) &= \Re \{ \tilde{\vec{v}}_1(\vec{r}) e^{-i\omega t} \}\end{aligned}\tag{11}$$

Eq. (10) reduces to a Helmholtz equation, given by

$$\nabla^2 p_1 - \frac{\omega^2}{c_0^2} p_1 = 0\tag{12}$$

It is worth noting that the harmonic vibration of the cantilever is the only necessary source for the acoustic perturbation. Since the equation governing the first order density  $\rho_1$ , pressure  $p_1$  and fluid velocity field  $v_1$  is linear, all first order parameters will be proportional to  $A$ . Therefore, the kinetic and potential energy terms from the first-order acoustic fields,

$$\begin{aligned}w_v &= \frac{1}{2} \rho_0 v_1^2 \\ w_p &= \frac{1}{2} \frac{p_1^2}{\rho_0 c_0^2}\end{aligned}\tag{13}$$

will have  $\sin^2(\omega t)$  or  $\cos^2(\omega t)$  dependence as well as  $A^2$ , similar to the energy terms shown in Supplementary Table 1. Therefore, when equating the total kinetic energy and potential energy (Rayleigh Ritz Theorem) to obtain the resonant frequency of the system, terms with  $A^2$  effectively cancels out. In fact, we have experimentally seen that amplitude does not affect our node deviation signal (Supplementary Fig. 3). It is clear that since  $p_1$  is in-phase with the cantilever vibration ( $\propto \cos(\omega t)$ , Supplementary Fig. 1b),  $\omega_p \propto \cos^2(\omega t)$  and will therefore contribute to the

potential energy of the system, as expected. On the other hand,  $v_1$  is out-of-phase with the cantilever movement ( $\propto \sin(\omega t)$ ), Supplementary Fig. 1c,d),  $\omega_v \propto \sin^2(\omega t)$  and will contribute to the total kinetic energy of the system. Next, we shift our discussion to the fluid-particle interaction, where a particle scatters the acoustic field around it, causing nearby fluid velocity and pressure to be

$$\begin{aligned}\vec{v}_1 &= \vec{v}_{in} + \vec{v}_{sc} \\ p_1 &= p_{in} + p_{sc}\end{aligned}\tag{14}$$

where  $\vec{v}_{in}$  and  $p_{in}$  are incident acoustic terms and  $\vec{v}_{sc}$  and  $p_{sc}$  are scattered terms. This will cause not only the acoustic fields to be scattered but the particle in the acoustic field to gain kinetic energy  $T_p$  and potential energy  $U_p$  related to the elastic deformation of the particle. Following the time-harmonic assumption, the gained kinetic energy can be obtained, as shown in Supplementary Table 1.

#### 1.4 Revised theory incorporating acoustic effects

We incorporate all acoustic energy terms, including those resulting from fluid-particle interactions in to Eq. (3) and Eq. (4) in order to derive the resonant frequency change of the SMR.

$$\begin{aligned}U_{total} &= U_{sil} + U_f + U_p \\ T_{total} &= T_{sil} + T_f + T_p\end{aligned}\tag{15}$$

where  $U_f$  and  $U_p$  denotes acoustic potential energy and stored elastic energy of the particle, respectively. For sufficiently small changes in the frequency ( $\Delta\omega \ll \omega_0$ ),

$$\begin{aligned}U_{total} &= U_0 + \Delta U(y) \\ T_{total} &= \alpha(\omega_0 + \Delta\omega)^2 + \Delta T(y)\end{aligned}\tag{16}$$

where  $U_0$  and  $T_0 = \alpha\omega_0^2$  are the time-averaged potential and kinetic energy of the system without the particle immersed in the SMR (i.e.,  $y=0$ ), respectively.  $\Delta U(y)$  and  $\Delta T(y)$  refer to change in potential and kinetic energy of fluids and particles, respectively, as a function of the particle position,  $y$ .

Applying the Rayleigh Ritz Theorem leads to:

$$\begin{aligned}\frac{\Delta\omega}{\omega_0} &= -1 + \left[1 - \frac{\Delta T(y) - \Delta U(y)}{U_0}\right]^{1/2} \\ &\simeq \frac{\Delta U(y) - \Delta T(y)}{2U_0}\end{aligned}\tag{17}$$

Eq. (17) generalizes the resonant frequency change of the system upon particle loading to be dependent on the total potential and kinetic energy of the system, unlike in Eq. (1), where frequency only depends on the particle position and mass. It is clear from Eq. (17) that even when a particle is located at the node with zero net out-of-plane motion, the disruption of the acoustic field would still result in a non-zero frequency shift.

The simulation results shown in Fig. 1d,e and Supplementary Fig. 2 was computed using the Eq. (17). This was accomplished by first numerically solving the Helmholtz equation (Eq. (12)) to obtain three fluid parameters (i.e.,  $\rho$ ,  $v$ ,  $p$ ), while varying the position of the particle along the channel. Then, we obtained the kinetic energy and potential energy of the system for each position (Supplementary Table 1), and subtracted the corresponding energy without the particle to get the term  $\Delta U(y) - \Delta T(y)$ . In Supplementary Note 2 we will discuss the necessary details of the simulation as well as provide more details for computing Eq. (17).

## Supplementary Note 2. Simulation

When the acoustic domain of interest has non-trivial geometry with complicated boundary conditions, solving the governing equations analytically is challenging. Therefore we utilize Finite Element Method (FEM) simulations<sup>4</sup> to solve the relevant equations provided in Supplementary Note 1. For FEM analysis, the governing equation (i.e., Wave equation: Eq. (10) for the time domain; Helmholtz equation: Eq. (12) for frequency domain) is to numerically solve for each individual 'block' within a mesh. In this note, we describe how the model is established and provide details on the post processing.

### 2.1 Geometry

For FEM analysis, COMSOL Multiphysics software 4.3 was used. The exact geometry of the SMR used for experiments in this work was reproduced in the software implementing the CAD design of SMR (Supplementary Fig. 1a and Supplementary Table 2). We embedded a particle in the detection regime of the cantilever (i.e., buried channel which is covered with thin silicon layers) and parameterized the y-position of the particle. We assumed the particle to be perfectly spherical, except where the effect of particle shape was tested. All dimensions used in the simulations are listed in Supplementary Table 2.

### 2.2 Model Setup

We used the 3-dimensional "Acoustic-Structure Interaction" module in the frequency domain provided by the software. The mathematical details of the governing equation and boundary conditions for the simulation are included in the manual<sup>4</sup>.

There are multiple possible sources that generate acoustic standing waves, but most of them will be second or higher order terms in the acoustic parameters (e.g., centrifugal force acting towards the tip and node). Here we neglect higher order acoustic sources and focus on the first order term, which is created by the out-of-plane motion of fluid channel in the cantilever, as given in Eq. (2).

$$a_t \equiv \ddot{z} = \omega^2 Au(y) a_b \equiv \ddot{z} = -\omega^2 Au(y) \quad (18)$$

where  $a_t$  and  $a_b$  are acceleration of the top and bottom surface, respectively. All simulations except viscous sphere model were performed under *pressure acoustics model*  $\rightarrow$  *fluid model*  $\rightarrow$  *linear elastic*. We used *sound hard boundary (wall)* condition for the fluid-channel boundary because of the high elastic modulus ( $> 10^{11}$  Pa) and acoustic impedance of the silicon surrounding the fluid channel. We obtained the same results by using a boundary condition that accounts for the silicon elastic modulus (data not shown). We assumed the entire particle (and shell region for Cortical Shell – Liquid Core model) to be a *linearly elastic material* and *isotropic* solid. COMSOL then solves for the elastic solid-acoustic interaction, which incorporates the re-radiation of the acoustic field by the vibration of the solid interface driven by the incident pressure field. For the cell model, we treated the inner liquid core as a fluid with density  $\rho = 1.05$  g/cm<sup>3</sup> and sound velocity similar to salt water of the same density. We used the default *free tetrahedral* meshing for the entire geometries (Supplementary Table 2), except for the thin shell when performing simulation of the cell models, where we first meshed the outer surface with *free triangular* and used a sweep function towards the inner surface with *number of elements* set to 10. The mesh size of the *free triangular* and *free tetrahedral* mesh was set using the *general physics* option *extremely fine* and *fluid dynamics* option, *finer* respectively. Using these options, the minimal edge length of a typical element was set to 0.105  $\mu$ m for outer surface meshing of the particle and 0.285  $\mu$ m for the rest of the geometry. The position of the particle or cell in the y-direction was *parameterized* with steps of 5-10  $\mu$ m along the length of the cantilever to effectively capture the shape of the frequency response and enable the comparison with experimental data (Fig. 1d,e). The center of mass was positioned in the center of the channel for the all the simulations excluding the ones when we investigated how SNACS is affected by the positional offset from center of the channel (Supplementary Fig. 6).

### 2.3 Post Processing

Once COMSOL finished solving for the acoustic parameters as well as particle kinetics and elastic deformation, we integrated parameters (e.g. velocity, deformation) over specific geometries to obtain each energy term (Eq. (15)) as a function of the particle position (Supplementary Table 1). Once all energy terms were calculated as a function of the particle position, we then exported the data to MATLAB. To obtain  $\Delta T(y)$  and  $\Delta U(y)$ , we subtracted all energy terms when the particle is at position  $y = 0$ , from the energy terms when the particles is at position  $y$ ;

$$\begin{aligned}\Delta U(y) &= (U_f(y) + U_{p,s}(y) + U_c(y)) - (U_f(0) + U_p(0) + U_c(0)) \\ \Delta T(y) &= (T_f(y) + T_{p,s}(y) + T_c(y)) - (T_f(0) + T_p(0) + T_c(0))\end{aligned}\quad (19)$$

where  $U_{p,s}$  and  $T_{p,s}$  denote the potential and kinetic energy, respectively, of the whole particle or the shell region of the cell model. The average deformation of the cell or particle was calculated assuming isometric expansion (i.e.,  $U_{p,s} = EA\Delta x^2/2x$ , where  $E$  is elastic modulus,  $A$  is the surface area of the cell or particle and  $x$  is the length before deformation,  $\Delta x$ ).  $U_c$  and  $T_c$  only apply to the cell model, where encapsulated inner core was treated as a fluid.

Lastly, to directly compare simulations with experiments, we converted the energy difference (in units of Joules, Eq. (19)) to a frequency shift (in units of Hz, Eq. (17)). To do this, we ran 10  $\mu\text{m}$  polystyrene beads in both simulations and experiments and calibrated the energy difference ( $\Delta U(y) - \Delta T(y)$ ) simulated when the bead is at the antinode ( $y = y_{an}$ ) with the resonant frequency shift measured experimentally at the antinode ( $\Delta f/f(y_{an})$ ).

### 2.4 Different mechanical models for cells

We also tested models other than the Cortical Shell – Liquid Core model, such as the Viscous Drop, the Acoustic Impedance Mismatch and the Bulk Elastic (Supplementary Table 3). For the Bulk Elastic model, the assumption of a uniform *linearly elastic material* was used. For Acoustic Impedance Mismatch, we assumed the cell to be a liquid sphere, with acoustic impedance set under the *Impedance* option. The Viscous Drop and Cortical Shell – Liquid Core model (Supplementary Fig. 5b) with the viscous core were simulated by selecting the *viscous fluid model* under *pressure acoustics model* while parameterizing the *dynamic* and *bulk viscosity* of the entire sphere or the fluid core of the Cortical Shell – Liquid Core. To simulate the effect of cytoplasmic pressure in our Cortical Shell – Liquid Core model (Supplementary Fig. 5c), we set the *pressure* under *initial values* to be parameterized within the range of 0-1000 Pa. The cortical tension model (Supplementary Fig. 5d) was developed similarly to previously reported COMSOL model<sup>5</sup>. Briefly, we applied a constant mechanical tension in the cortex by assigning an *initial stress* to the shell domain under *initial stress and strain*. Using Laplace's relationship, we assigned the *initial stress* in spherical coordinate ( $\rho, \theta, \varphi$ ; relative to the center of the liquid core) as

$$\begin{bmatrix} 0 & 0 & 0 \\ 0 & pr_c/2t_s & 0 \\ 0 & 0 & pr_c/2t_s \end{bmatrix}\quad (20)$$

where  $p$  is the internal pressure,  $r_c$  is the cell radius, and  $t_s$  is the shell thickness.

## Supplementary Note 3. Correcting mass distribution

### 3.1 Deconvolution of mass and acoustic signal

As we showed in the previous notes, the resonant frequency shift of the SMR at any point in time due to a particle present in the integrated channel is a superposition of the frequency change due to the added particles mass and acoustic scattering created by the particle (Supplementary Fig. 2),

$$\Delta f_{measured} = \Delta f_{mass} + \Delta f_{acoustic} \quad (21)$$

Here we assume  $\Delta f_{mass}$  is the frequency shift caused by a point-mass particle as shown in Eq. (1), which is proportional to the squared amplitude dependence of the mode shape,  $u^2(y)$ . However, a particle with a mass distribution along the cantilever would cause a frequency shift deviating from the squared mode shape. Therefore, in order to obtain the shape-insensitive acoustic term,  $\Delta f_{acoustic}$ , we need to correct for the mass distribution,  $\Delta f_{mass}$ , affecting  $\Delta f_{measured}$ . Here, we ignore the contribution of acoustic effects to the frequency shift and discuss only the contribution of the mass distribution to the resulting frequency shift. If a particle of length  $2L$  with a linear mass distribution,  $\lambda(x)$ , is located at the position  $y$  along the cantilever, the shift in the resonant frequency is given by

$$\Delta f_{mass}(y) = \Delta f_{measured}(y_{an}) \frac{\int_{-L}^L \lambda(x) u^2(y+x) dx}{\int_{-L}^L \lambda(x) u^2(y_{an}+x) dx} \quad (22)$$

where  $y_{an}$  is the position of the antinode and  $\Delta f_{measured}(y_{an})$  is the measured frequency shift at the antinode (i.e., buoyant mass). Although a point mass would create no mass-dependent frequency shift at the node ( $y_n, u(y_n) = 0$ ), a particle with a non-zero size along the length of the cantilever will create a non-zero frequency shift when it is centered at the node. This contribution can be calculated from Eq. (22), and thus a correction can be made provided the size, shape and mass of the particle is known. The list of mass distributions,  $\lambda(x)$ , for some of the geometries that we encountered during this work is shown in Supplementary Table 4. For simplicity, we assumed the mass is homogeneously distributed around the geometry. As expected, compared to the single spherical particle, a doublet of particles will result in a larger frequency shift due to mass elongation. Although spheres have positional invariance making  $\lambda$  invariant to particle rotation, the  $\lambda$  for a doublet depends on its orientation relative to the cantilever (Supplementary Table 4).

### 3.2 Correction for cell elongation in anaphase

During the transition from a singlet to a doublet during anaphase, we assume that the total volume remains constant and that all geometries are the result of an overlap of two equally sized spheres (Supplementary Fig. 9). To accomplish this, we numerically solve for an individual sphere radius,  $r_t$ , with total elongation length,  $L$ , and volume,  $V$ , matching the following conditions:

$$\begin{aligned} L &= 4r_t - d \\ V &= 2 \int_{-r_t}^{r_t-y/2} \pi(r_t-x)^2 dx \end{aligned} \quad (23)$$

where  $d$  is the length of intersection between two identical spheres (Supplementary Table 4). With  $r_t$  obtained above, we add the following frequency shift to the node deviation we measured to correct for the mass elongation effect.

$$\Delta f_{correction}(y_n) = \Delta f_{measured}(y_{an}) \left[ \frac{\int_{-L/2}^{L/2} \lambda_t(x) u^2(y_n+x) dx}{\int_{-L/2}^{L/2} \lambda_t(x) u^2(y_{an}+x) dx} - \frac{\int_{-r_s}^{r_s} \lambda_s(x) u^2(y_n+x) dx}{\int_{-r_s}^{r_s} \lambda_s(x) u^2(y_{an}+x) dx} \right] \quad (24)$$

where  $y_n$  is position of the node and  $\lambda_t$  and  $\lambda_s$  refer to the linear mass distribution of the overlapping spheres of individual radii of  $r_t$  and singlet of radius  $r_s$ , respectively (Supplementary Table 4). However, since  $\lambda_t$  depends on the exact orientation relative to the channel, there will be an error estimating the frequency shift,  $\Delta f_{correction}$ . For all data shown throughout this work, we assumed that the cells are oriented by an intermediate angle (i.e.,  $\theta_{max}/2$ ) during late mitosis (Supplementary Fig. 15). We further discuss the details of such orientation-dependent error in Supplementary Note 4.

## Supplementary Note 4. Orientation-dependent noise

Orientation of a particle relative to the channel can affect mass distribution along the channel and result in a SNACS that is independent of the mechanical properties (Supplementary Note 3 and Supplementary Table 4). For example, the SNACS from a cylindrical particle flowing parallel through the channel at the node will be different from the case where the same particle has a perpendicular orientation (Supplementary Table 4, 1st and 2nd row, respectively). Thus, for non-spherical particles, the SNACS measurement contains an intrinsic noise that results from an uncertain orientation during detection at the node. For suspension cells, the shape is generally spherical up until late mitosis and so the orientation noise is negligible. This is evident by the low noise in our SNACS measurement during interphase (Fig. 3a,b).

For cells that deviate from a spherical shape, a spurious SNACS signal could arise if the cell gradually changes its orientation as it flows back-and-forth through the channel. There are two approaches for determining if a signal is spurious. The first applies to situations where the time range of a possible mechanical change is known (e.g. during mitosis). In this case, the SNACS signal can be measured from multiple cells. The resulting signals can be aligned and an analysis for statistical significance can be performed (for example Fig. 3c, where mitotic cells were aligned at the metaphase-anaphase transition). If a cell's orientation should gradually drift during a measurement, it will not be correlated across different cells.

The second approach applies to situations where changes in mechanics occur stochastically. In this case, the error resulting from orientation noise must be quantified. A threshold can then be established for determining if the SNACS measurement is revealing statistically significant changes in cell mechanics. The maximum orientation error in node deviation ( $\Delta ND_{orientation}$ ) can be calculated provided the cell shape is known (e.g. by DIC imaging),

$$\Delta ND_{orientation} = \Delta f_{mass,or1}(y_n) - \Delta f_{mass,or2}(y_n) \quad (25)$$

where  $\Delta f_{mass}(y_n)$  is given in Eq. (22). If the change in SNACS is sufficiently larger than the error obtained from Eq. (25), the resulting signal will be associated with changes in cell mechanics. We next present three examples to illustrate how orientation noise is estimated.

### 4.1 Cylindrical geometry

For a cylindrical particle of radius  $r$  and length  $L$ , the maximal node deviation change due to orientation error given by Eq. (25) is

$$\begin{aligned} \Delta ND_{orientation} &= \Delta f_{mass,c\parallel}(y_n) - \Delta f_{mass,c\perp}(y_n) \\ &= \Delta f_{measured}(y_{an}) \left[ \frac{\int_{-L/2}^{L/2} \lambda_{c\parallel}(x) u^2(y_n + x) dx}{\int_{-L/2}^{L/2} \lambda_{c\parallel}(x) u^2(y_{an} + x) dx} - \frac{\int_{-r}^r \lambda_{c\perp}(x) u^2(y_n + x) dx}{\int_{-r}^r \lambda_{c\perp}(x) u^2(y_{an} + x) dx} \right] \quad (26) \end{aligned}$$

where,  $\lambda_{c\parallel}, \lambda_{c\perp}$  is mass distribution function of a cylindrical sample lying parallel and perpendicular to the channel, respectively. From Eq. (26), a cylindrical hydrogel with a 10  $\mu\text{m}$  diameter, 8  $\mu\text{m}$  height and  $\Delta f_{measured}(y_{an}) = 17 \text{ Hz}$ , the resulting orientation noise is  $\sim 0.004 \text{ Hz}$ , which is equivalent to SNACS noise of  $\sim 0.006$  (a.u.).

### 4.2 Cells in late mitosis

Here we estimate the orientation noise of a cell in late mitosis. Specifically, we use Eq. (25) to calculate the maximum error from orientation uncertainty as the cell elongates. Similar calculation done for the cylindrical hydrogel shown in Supplementary Note 4.1 will be performed. However, since the length of the elongated cell is greater than the channel width, the maximal rotation is now constrained. For example, overlapping spheres of total elongation length



$L$ , and individual radius  $r_t$  flowing through the channel of width  $w$  can only rotate by an angle  $\theta$  from  $y$ -axis (i.e. direction of a particle/fluid flow through the cantilever) (Fig. 1a and Supplementary Fig. 1a) which is given by,

$$2r_t + (L - 4r_t) \sin(\theta_{max}) = w \quad (27)$$

Using  $w = 20 \mu m$  for our cantilever and the maximal angle provided from Eq. (27), Supplementary Fig. 15a bounds the maximum error due to orientation uncertainty as the cell elongates. Initially the error increases as the cell elongates. At a critical elongation length, the error reaches a maximum because the rotation within the channel begins to be constrained ( $\theta_{max} < 90^\circ$ ).

### 4.3 Effect of sample orientation uncertainty on measured and corrected SNACS

In Supplementary Note 3, we described how to correct the SNACS signal for changes in mass distribution obtained by simultaneously measuring cell shape. Here, with the goal of showing the interplay between Supplementary Notes 3 and 4, we show the expected SNACS signal from a hypothetical cell that elongates during mitosis. In one case, we allow the mechanical properties to remain constant during elongation (Supplementary Fig. 15b, top panel, left), and for the other case, to change in a fashion similar to what we've observed in L1210 cells (Supplementary Fig. 15b, top panel, right). As shown in previous note (Eq. (22)), elongation causes the measured SNACS signal to be decreased due to mass distribution changes, but also variable depending on the orientation relative to the channel. The SNACS decrease and increased noise are independent from the cell's mechanical properties (Supplementary Fig. 15b, middle panel; gray area bounded by red and blue dashed line). In other words, SNACS measured at any given time point can fall along the gray region in Supplementary Fig. 15b middle panel. If we then apply the mass distribution correction scheme discussed in Supplementary Note 3 to the expected SNACS curves, we recover the trajectory where our error is determined by the upper and lower bound calculated from the orientation (Supplementary Fig. 15b, bottom panel; gray area bounded by red and blue dashed lines). It is clear that our orientation-dependent noise is small enough to distinguish cellular mechanical changes observed in mitotic L1210 cells (Supplementary Fig. 15b, right) from the hypothetical constant case (Supplementary Fig. 15b, left).

### Supplementary Note 5. Swelling driven cortical expansion

Here we present the mathematics that govern the reduction of cortical thickness when the total volume expands. For this calculation, we assume that the volume expansion is isometric and that the cortical actin content and density does not change as a result of the expansion. Therefore, when a shell of thickness  $t_s$ , and total radius  $r_c$  (Figs. 2a and 4d) undergoes isometric volume expansion to bigger radius  $r'_c$ , the shell thickness would be reduced to  $t'_s$ ,

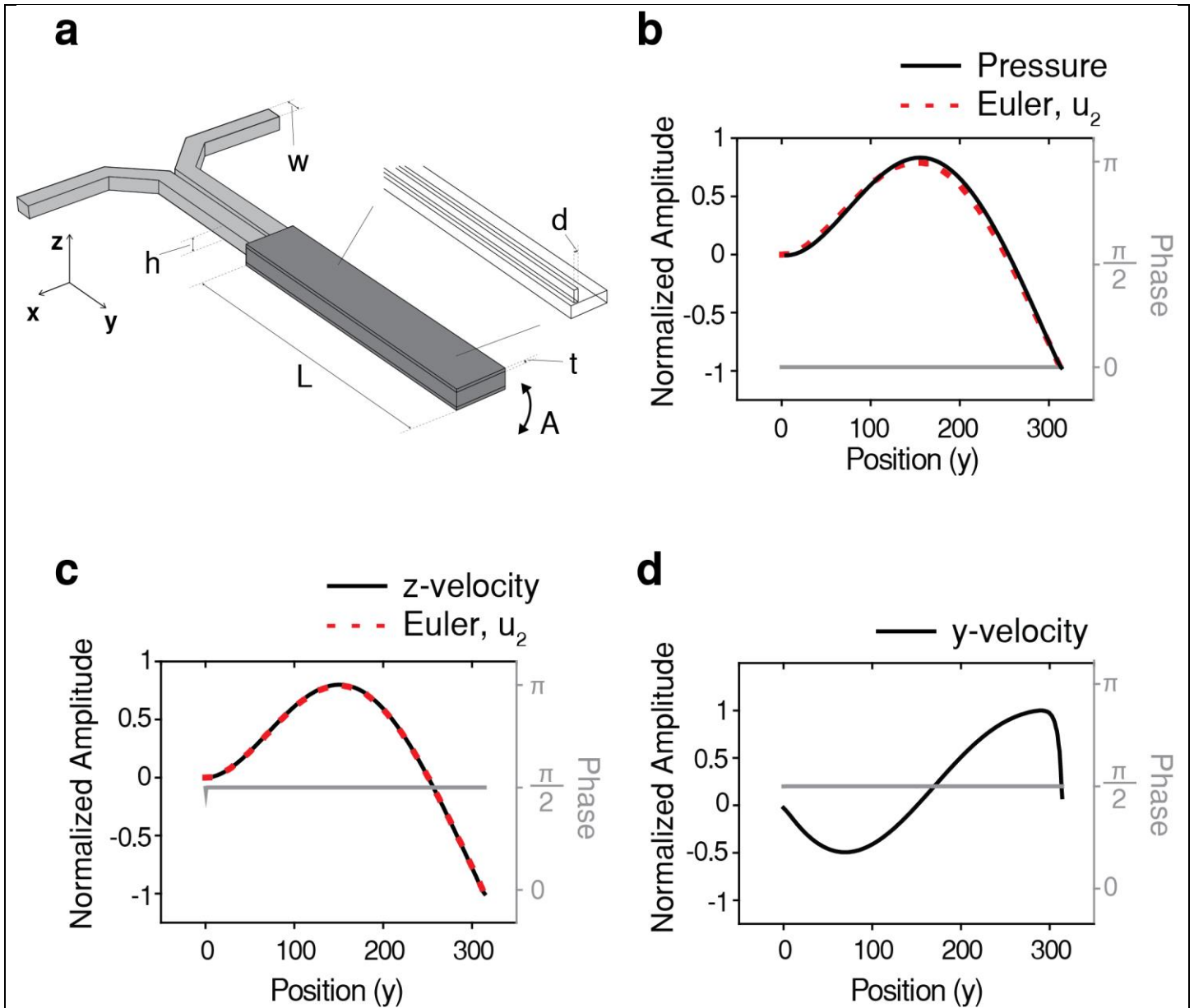
$$\frac{4}{3}\pi r_c^3 - \frac{4}{3}\pi(r_c - t_s)^3 = \frac{4}{3}\pi r'_c{}^3 - \frac{4}{3}\pi(r'_c - t'_s)^3 \quad (28)$$

Supplementary Table 5 lists some of the values that were calculated using Eq. (28).

Our FEM simulation revealed that increasing volume by 14.1% and, consequently, decreasing the cortex thickness to radius ratio by ~10% required an additional 10% decrease in cortical elastic modulus to match with the SNACS change we observe in early mitosis (Fig. 4c). This could be because cortical expansion during swelling causes actin cortex to be detached from the surface<sup>6</sup> or because F-actins get partially damaged or ruptured by an increase in intracellular pressure<sup>7</sup>.

## Supplementary References

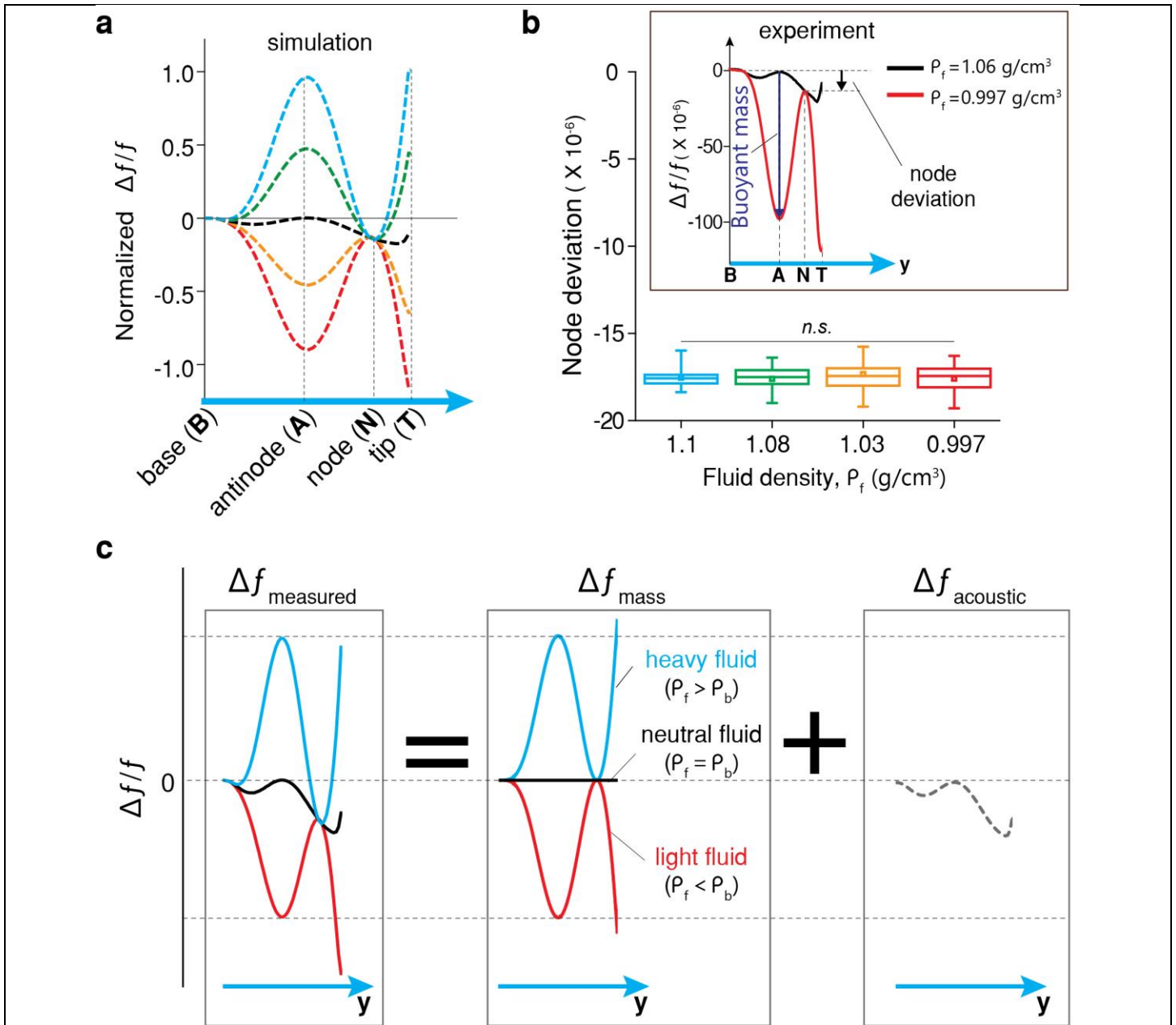
- 1 Dohn, S., Svendsen, W., Boisen, A. & Hansen, O. Mass and position determination of attached particles on cantilever based mass sensors. *The Review of scientific instruments* **78**, 103303 (2007).
- 2 Lee, J., Bryan, A. K. & Manalis, S. R. High precision particle mass sensing using microchannel resonators in the second vibration mode. *Rev Sci Instrum* **82**, 023704 (2011).
- 3 Bruus, H. Acoustofluidics 1: Governing equations in microfluidics. *Lab Chip* **11**, 3742-3751 (2011).
- 4 "COMSOL Multiphysics Reference Manual, version 4.3", COMSOL, Inc, [www.comsol.com](http://www.comsol.com).
- 5 Fischer-Friedrich, E. *et al.* Rheology of the Active Cell Cortex in Mitosis. *Biophysical journal* **111**, 589-600 (2016).
- 6 Steltenkamp, S., Rommel, C., Wegener, J. & Janshoff, A. Membrane stiffness of animal cells challenged by osmotic stress. *Small* **2**, 1016-1020 (2006).
- 7 Pritchard, S. & Guilak, F. The role of F-actin in hypo-osmotically induced cell volume change and calcium signaling in anulus fibrosus cells. *Ann Biomed Eng* **32**, 103-111 (2004).



Supplementary Figure 1

**SMR geometry and acoustic parameters from simulation.**

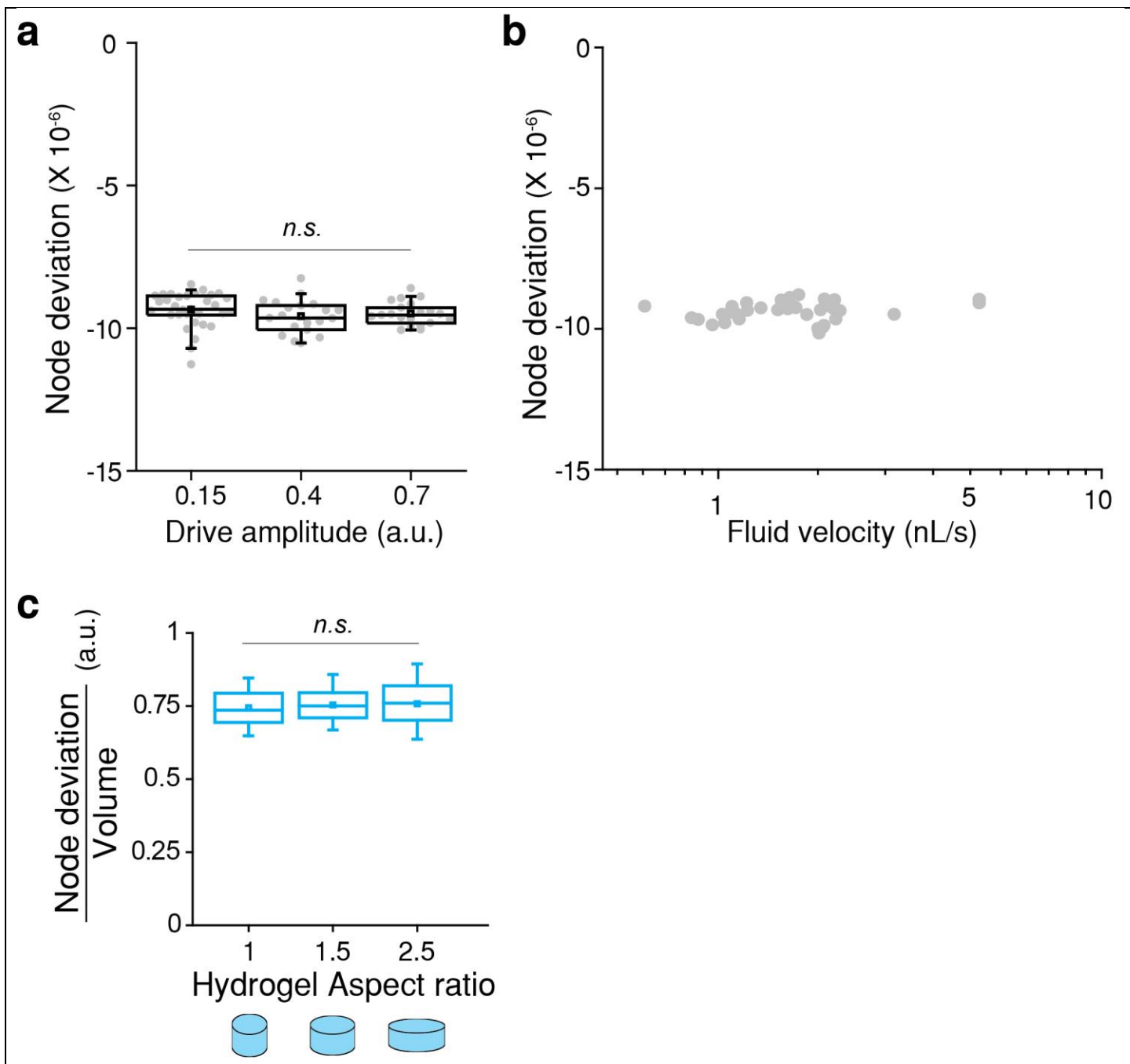
**a**, SMR geometry, dimensions (Supplementary Table 2) and coordinates. The fluid channel in the detection regime is covered with thin silicon layers (dark gray). Inset shows the buried channel. All dimensions are listed in Supplementary Table 2. **b-d**, Simulated acoustic pressure (**b**), z-velocity (**c**), and y-velocity (**d**). Amplitude (black) and phase (gray) are plotted along the top edge of the channel. The maximal amplitude of z-velocity and y-velocity were  $\sim 0.5$  m/s and  $\sim 0.075$  m/s, respectively. The 2<sup>nd</sup> mode shape from Euler-Bernoulli beam equation ( $u_2$ ) is plotted in red dashed line.



Supplementary Figure 2

**Node deviation is independent of the mass change.**

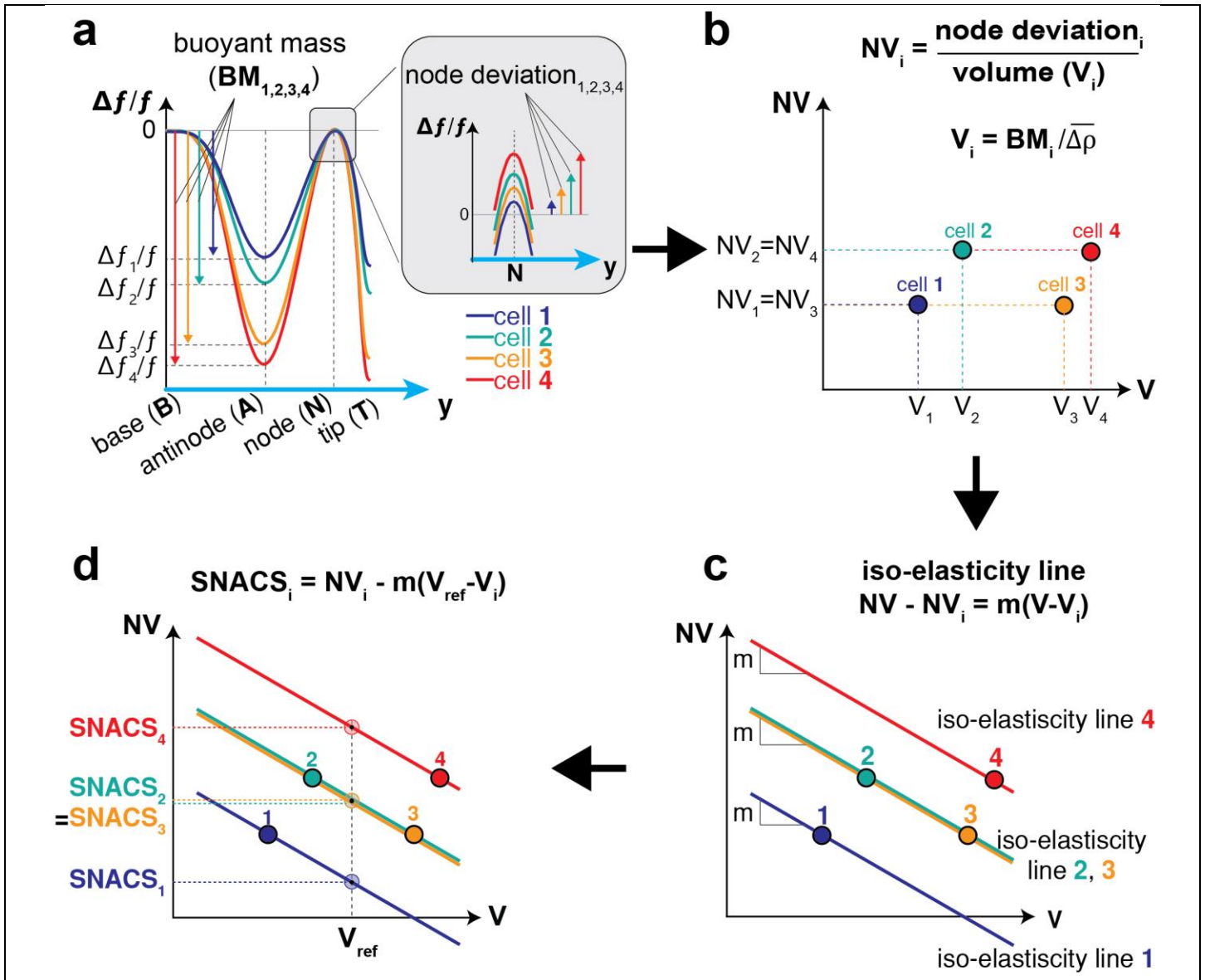
**a**, Frequency signals from simulations with 12  $\mu\text{m}$  polystyrene bead ( $\rho_b = 1.06 \text{ g/cm}^3$ ) immersed in fluids of different densities ( $\rho_f = 1.1, 1.08, 1.06, 1.03$  and  $0.997 \text{ g/cm}^3$  for blue, green, black, orange and red traces, respectively). Frequency signals were normalized relative to the result obtained for  $\rho_f = 1.1 \text{ g/cm}^3$  (blue). **b**, Node deviation from experiments with 12  $\mu\text{m}$  polystyrene bead immersed in fluids of same densities as in **a** (1.1, 1.08, 1.03 and  $0.997 \text{ g/cm}^3$ ,  $n = 17, 97, 84$ , and 120 beads, respectively with same colors as in **a**). Boxes: interquartile range, squares: mean, whiskers: 5-95%;  $P = 0.32$  (one-way ANOVA). n.s., not significant. Inset: overlay of the frequency signal obtained from the density-matched fluid ( $\rho_f = \rho_b = 1.06 \text{ g/cm}^3$ , black) and water ( $\rho_f = 0.997 \text{ g/cm}^3$ , red). Buoyant mass ( $\Delta m$ , blue arrow) and node deviation (black arrow) are highlighted. **c**, Conceptual illustration of the frequency response, which is a superposition of the frequency response caused by both mass change, and the acoustic term independent of mass.



**Supplementary Figure 3**

**Node deviation is not sensitive to SMR drive amplitude, particle flow velocity across the channel or particle shape.**

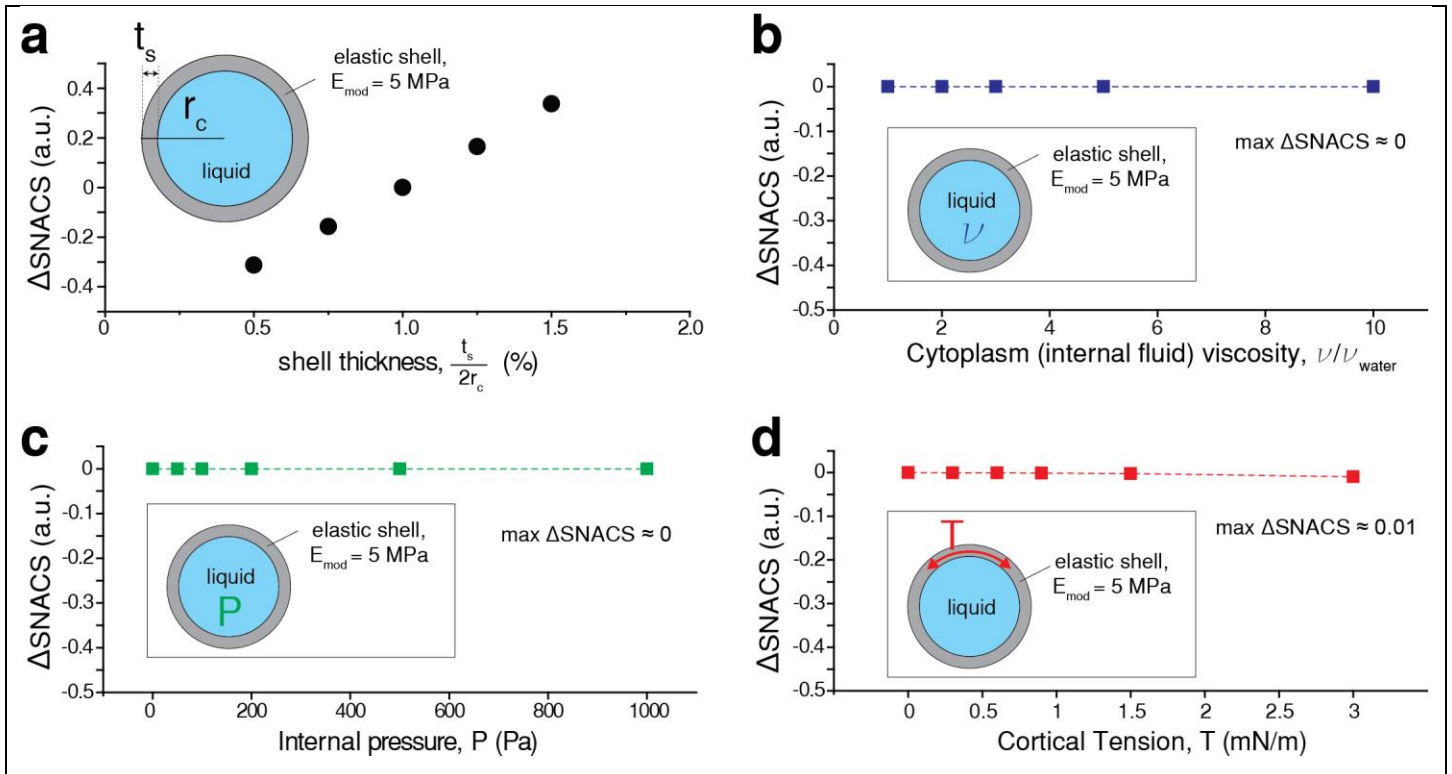
**a**, Node deviation from experiments with 10  $\mu\text{m}$  polystyrene beads measured by SMR vibrating in different amplitudes (0.15, 0.4 and 0.7,  $n = 33, 21$  and  $21$  beads, respectively).  $P = 0.37$  (one-way ANOVA). n.s., not significant. **b**, Node deviation from experiments with 10  $\mu\text{m}$  polystyrene beads measured by SMR with different fluid velocities ( $n = 35$  beads). Velocities were derived from transit time of the beads through the cantilever that is calculated from the duration of the resonant frequency shift of the beads. **c**, Node deviation vs aspect ratio (AR) from experiments with synthetic hydrogels of different shapes but same volume (AR 1, 1.5 and 2.5,  $n = 384, 423$  and  $474$  hydrogels, respectively).  $P = 0.10$  (one-way ANOVA). n.s., not significant. In **a,c**, boxes: interquartile range, squares: mean, whiskers: 5-95%.



Supplementary Figure 4

Illustration of the methodology used for obtaining the size-normalized acoustic scattering (SNACS) from the node deviation.

**a-b**, Steps for obtaining SNACS: The resonant frequency shifts ( $\Delta f/f$ ) for each cell (1-4, color curves) are used to measure the buoyant mass (BM) at the antinode and the node deviation at the node (**a**). Scatter plot of volume-normalized node deviation (NV) vs volume ( $V$ ) (**b**). The volume of each cell ( $V_{1,2,3,4}$ ) is obtained from the corresponding buoyant mass ( $BM_{1,2,3,4}$ ) using the included equation.  $\bar{\Delta\rho}$  is the median density of the population relative to the fluid. Data points of cells (1-4) are fit with iso-elasticity lines (color lines) with slope  $m$  (**c**). The slope ( $m$ ) was obtained by performing a linear regression on the population data in the NV vs  $V$  scatter plot shown in Fig. 2b. SNACS of each cell is obtained using the included equation (**d**). Graphically, the SNACS of each cell corresponds to a NV value at the intersection point between the iso-elasticity line (color lines) and the vertical line,  $V = V_{ref}$  (black dotted line), where  $V_{ref}$  is set to the median volume of the population. See Methods for additional details.

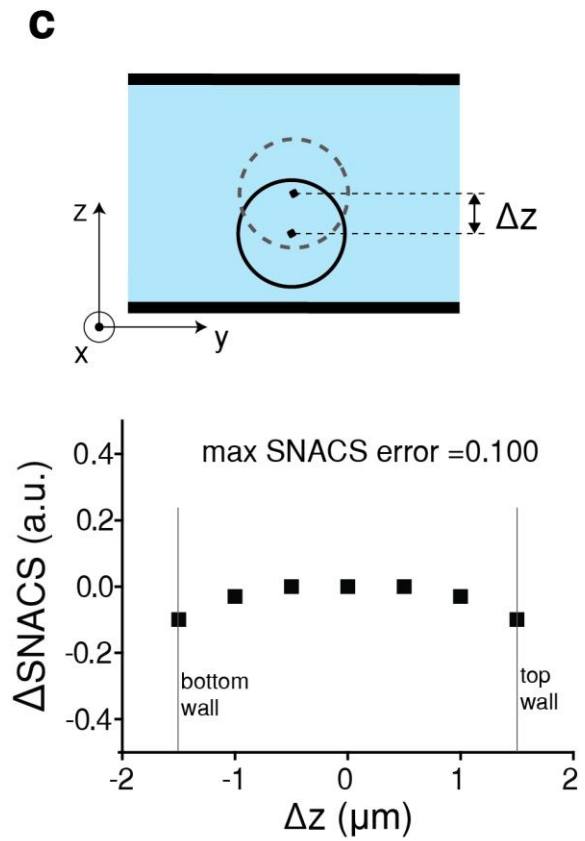
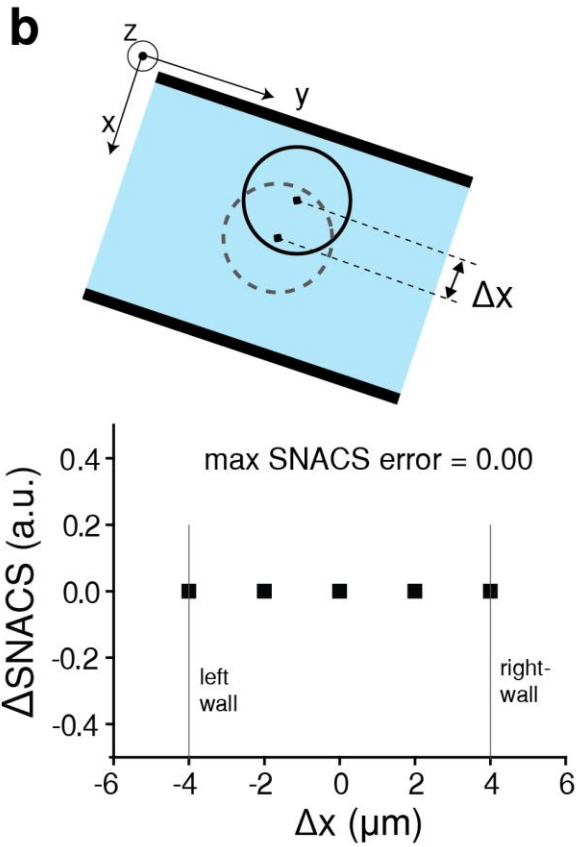
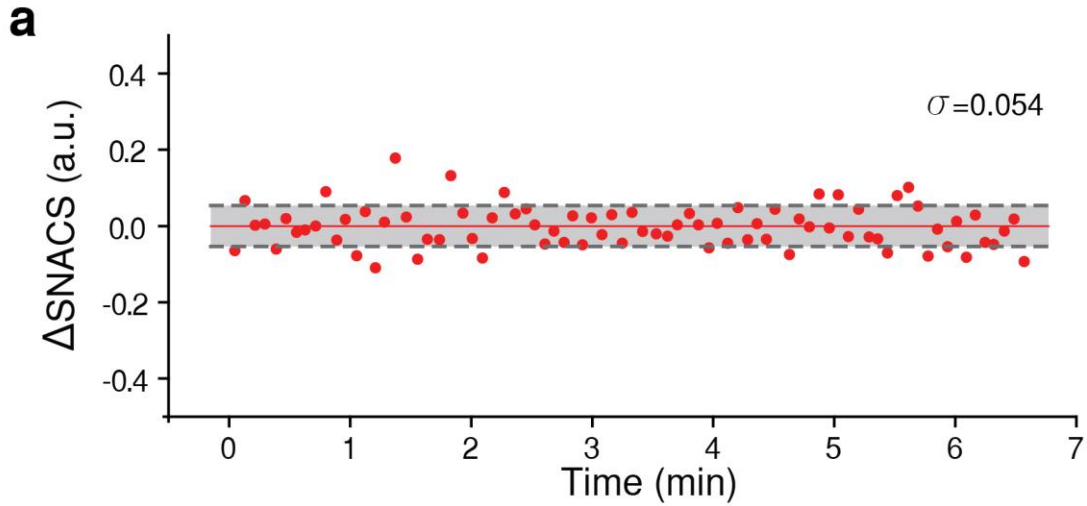


**Supplementary Figure 5**

**SNACS correlates with cortical thickness but is not sensitive to cytoplasmic viscosity, intracellular pressure or cortical tension based on FEM simulation on Cortical Shell-Liquid Core model.**

**a-d**, FEM Simulation results of SNACS obtained from the Cortical Shell – Liquid Core model upon changes in cortical thickness (**a**), cytoplasm (internal fluid) viscosity (blue) (**b**), internal pressure (green) (**c**), and cortical tension (red) (**d**). SNACS changes relative to  $\frac{t_s}{2r_c} = 1\%$ ,  $\nu/\nu_{water} = 1$ ,  $P = 0$ , and  $T = 0$  are plotted, respectively. Tension was simulated by applying initial stress to the elastic shell region, in-plane direction. See Supplementary note 2.4 for additional details. Insets, illustration of liquid-core elastic shell model with parameters being solved in FEM simulation. For all simulation, total radius ( $r_c$ ) and shell elastic modulus ( $E_{mod}$ ) were fixed at  $6 \mu\text{m}$  and  $5$  MPa, respectively.

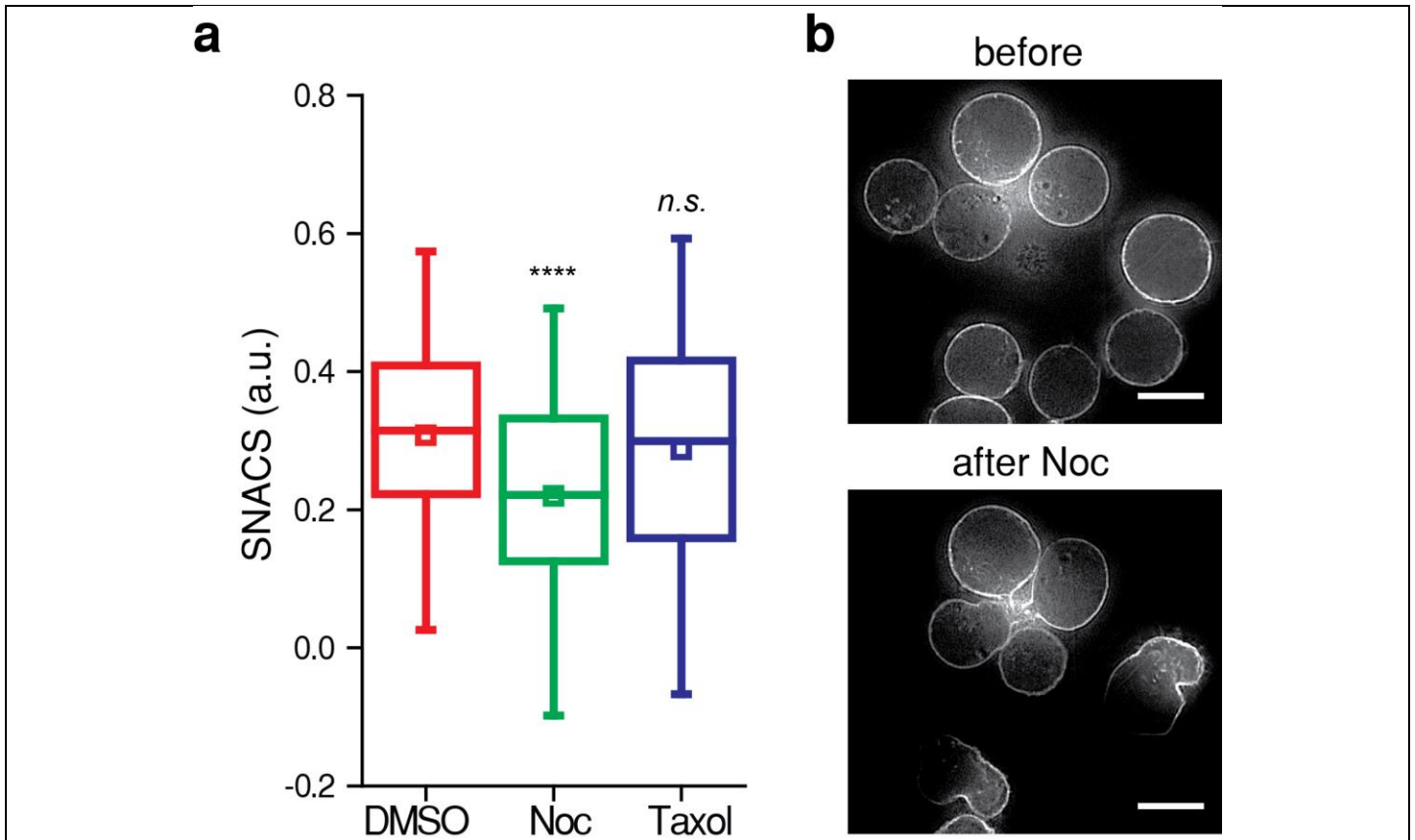




### Supplementary Figure 6

#### SNACS noise characterization.

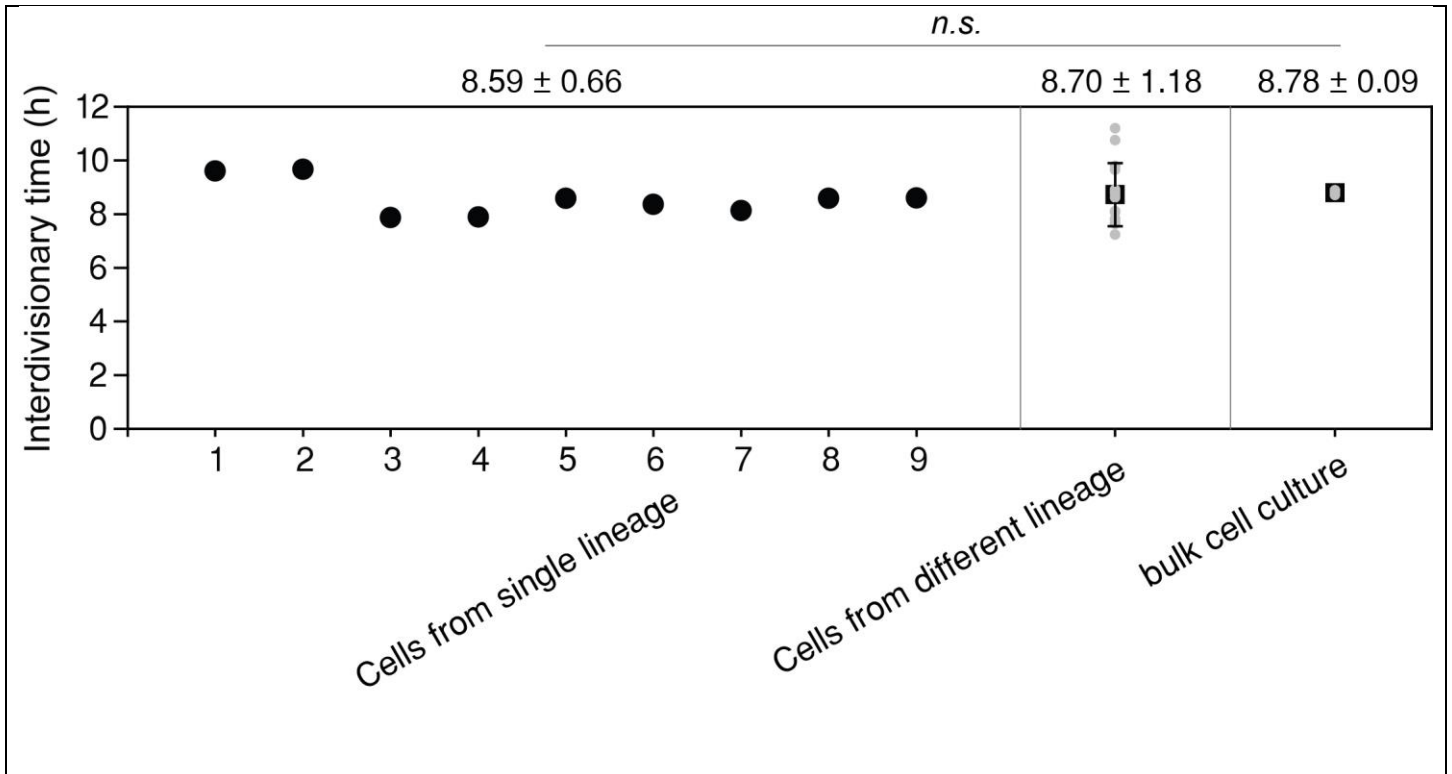
**a**, Continuous SNACS measurements of a single 12  $\mu\text{m}$  polystyrene bead ( $n = 79$  repeated measurements) implementing the same fluidic control strategy for continuous monitoring of single-cell SNACS (Fig. 3a). The mean (set to zero) is shown in red line and  $\pm$  s.d. ( $\sigma$ ) in gray dashed lines. Gray area marks the data region within  $\pm \sigma$ . **b**, **c**, Illustration (top) and simulation results (bottom) of the cell model (Fig. 2a) with total radius ( $r_c$ ) and shell elastic modulus ( $E_{mod}$ ) of 6  $\mu\text{m}$  and 5 MPa, respectively with x-positional (**b**) and z-positional (**c**) offset from center of the channel. Vertical lines mark the offset distance from the center to positions where the outer surface of the cell touches channel walls.



Supplementary Figure 7

**Microtubule perturbation affects actin cortex and SNACS.**

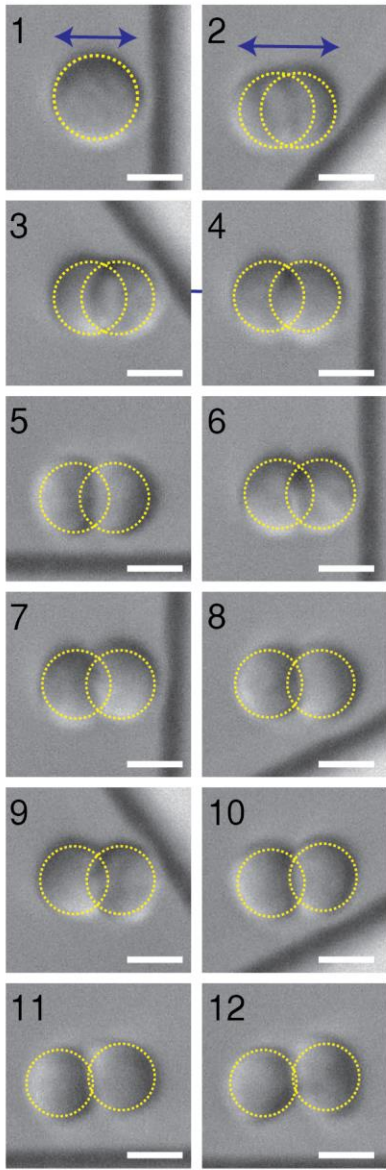
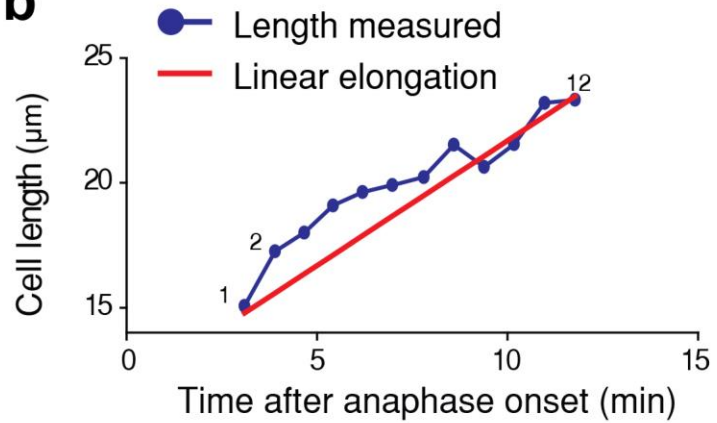
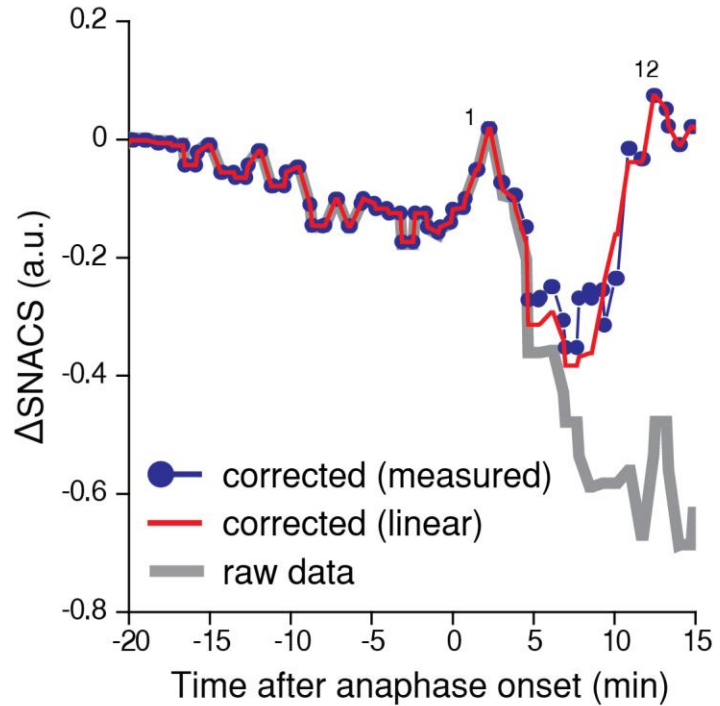
**a**, SNACS measured from L1210 cells treated with microtubule affecting drugs: Nocodazole (Noc, 1  $\mu\text{g/ml}$ ,  $n = 760$  cells,  $P = 2.8 \times 10^{-16}$ ) and Taxol (25  $\mu\text{M}$ ,  $n = 511$  cells,  $P = 0.12$ ). Statistical comparisons (two-sided Welch's t-test) were made to DMSO control (0.1 %,  $n = 718$  cells). Boxes: interquartile range, squares: mean, whiskers: 5-95%; \*\*\*\* $P < 0.0001$ , n.s., not significant. **b**, Representative images of actin cortex from live L1210 cells expressing LifeAct-RFP F-actin probe before (top) and after (bottom) Nocodazole 1  $\mu\text{g/ml}$  treatment ( $n = 7$  fields of views). Scale bars, 10  $\mu\text{m}$ .



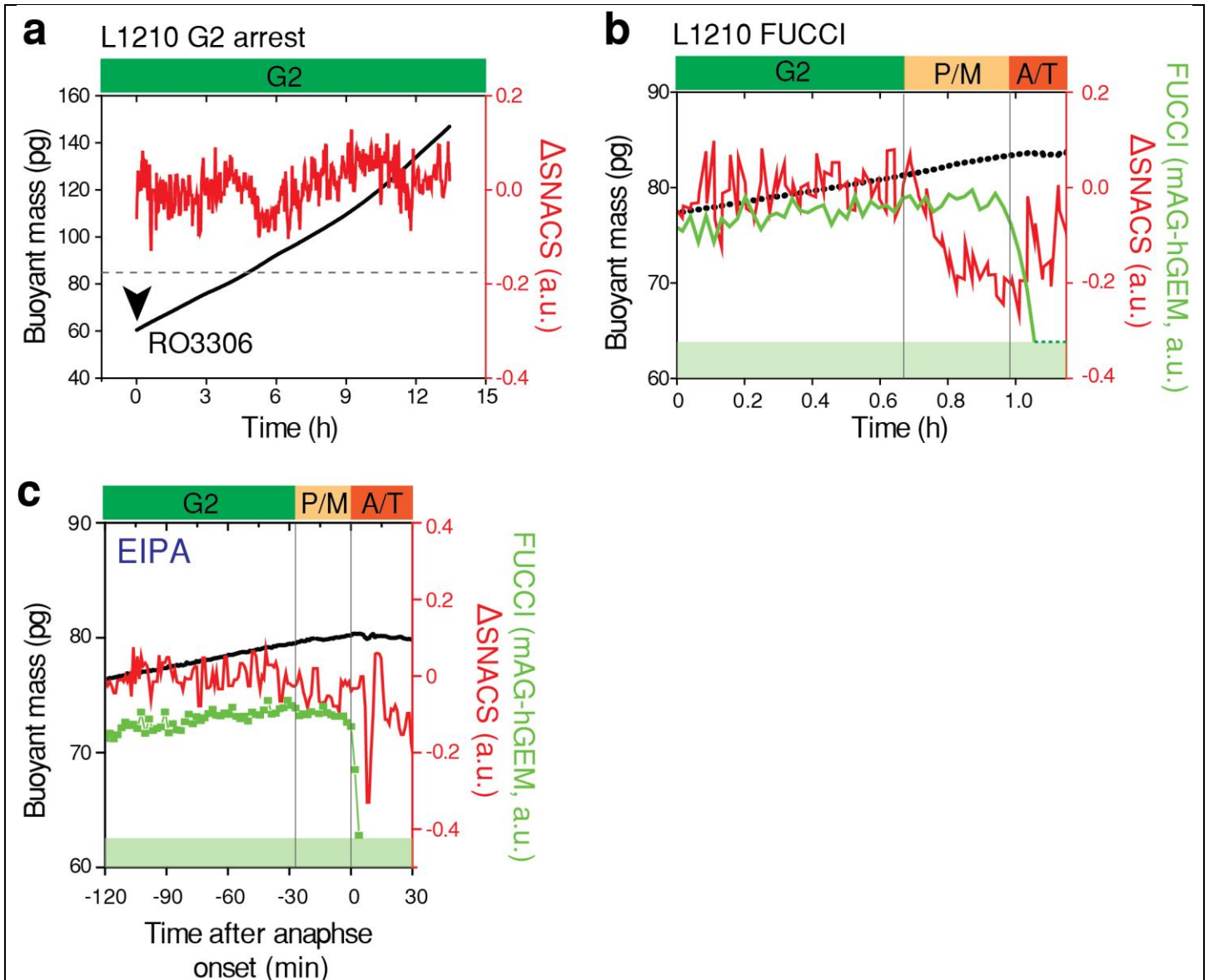
**Supplementary Figure 8**

**Continuous SNACS measurements do not affect interdivision time.**

Interdivision time (doubling time) of each daughter cell from the same lineage (left column, black dots), single cells from different lineage (middle column, gray dots) and from bulk cell culture (right column, gray dots). All single cells grown in SMR were exposed to the same conditions reported in the manuscript (SNACS measurement every 1 min). Higher temporal resolution can be achieved. However, repeating measurements more often than every 30 s may start to interfere with cell growth. For middle and right columns, data depicts mean  $\pm$  s.d. Each mean  $\pm$  s.d. is listed on top.  $P = 0.95$  (one-way ANOVA). n.s., not significant.

**a****b****c****Supplementary Figure 9****Illustration of mass distribution correction in late mitosis.**

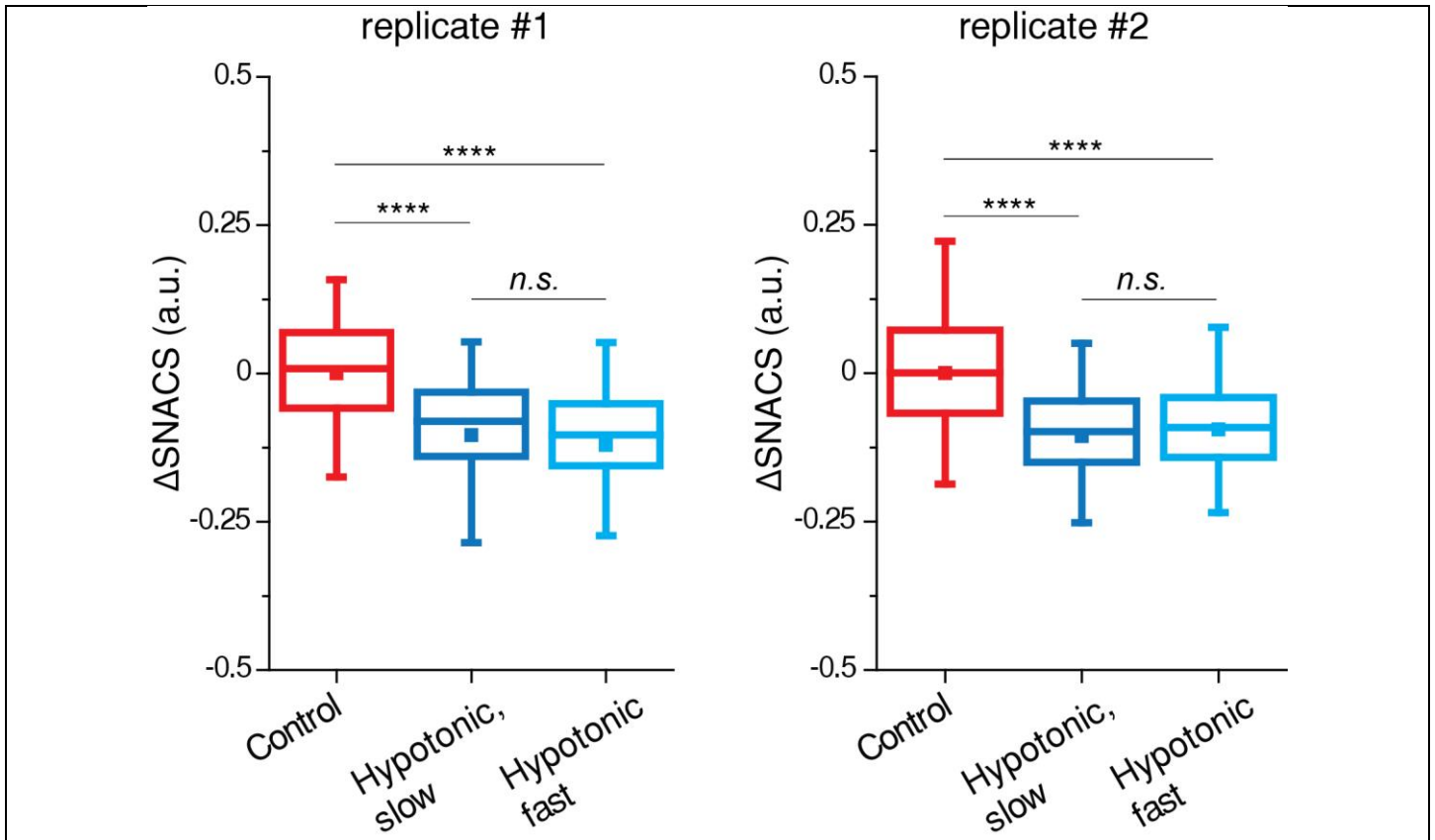
**a**, DIC images of the mitotic L1210 cell acquired on-chip, simultaneously with SNACS and buoyant mass measurement in late mitosis. For each time point, cells were fitted with overlapping spheres (yellow dotted lines) based on the measured elongation length (blue double arrows). Each number on the image marks the time progression. Scale bars, 10  $\mu\text{m}$ . **b**, Cell length measured (blue dots) is plotted as a function of time after onset of anaphase. Numbers correspond to the images shown in **a**. The linear elongation derived from the first (1) and last image (12) is shown in red line. **c**, SNACS before correction (gray), after correction for the mass elongation using length directly measured from DIC images (blue dots) and assuming linear elongation (red) are plotted as a function of time after onset of anaphase. Numbers correspond to the images in **a**. See Supplementary Note 3 for additional details.



**Supplementary Figure 10**

**SNACS change occurs in early mitosis and is reduced by EIPA treatment.**

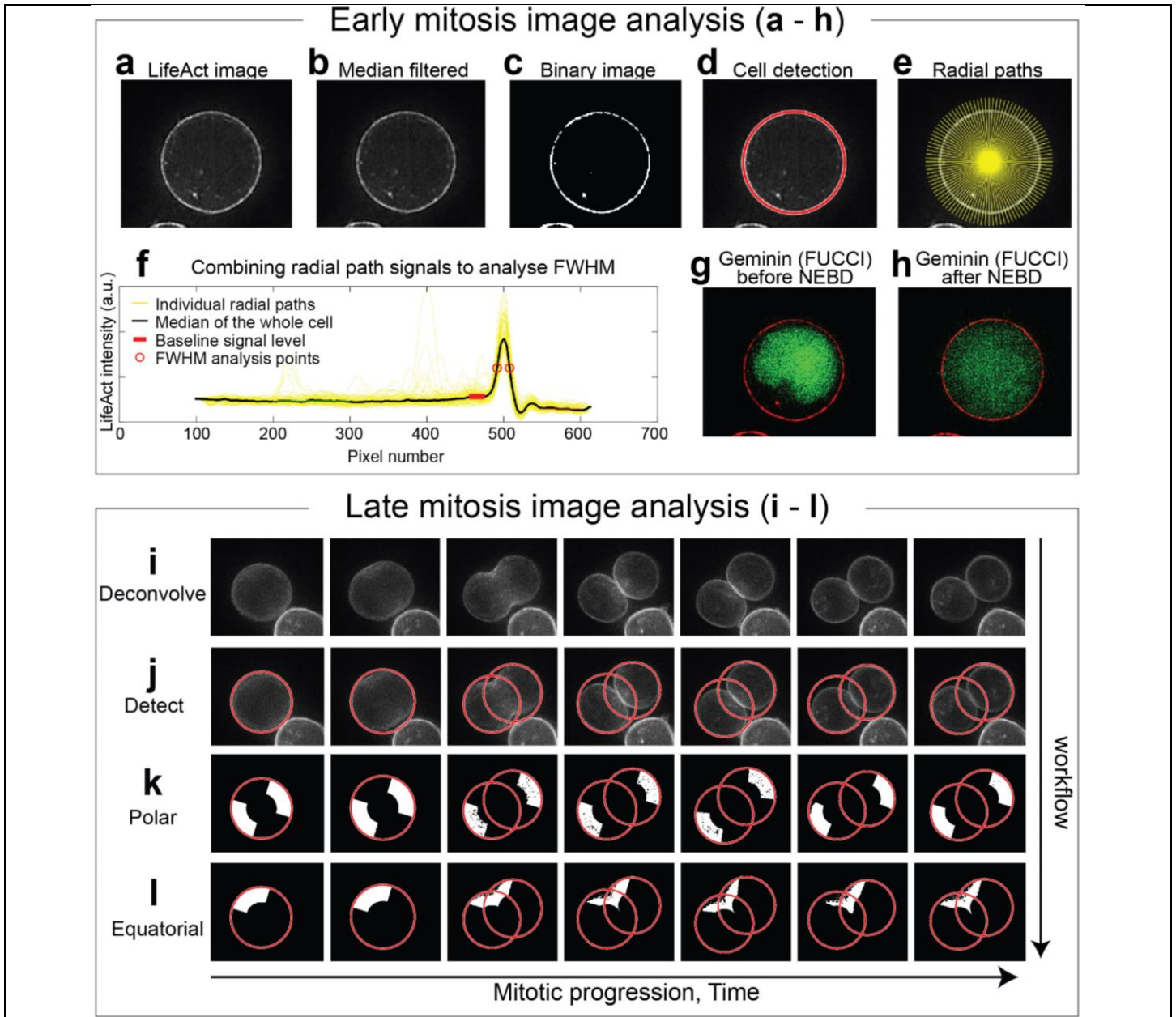
**a**, Buoyant mass (black) and SNACS (red) of L1210 treated with 2  $\mu$ M RO-3306, a CDK1 inhibitor. Arrow head marks the start of drug exposure. The cell arrested in G2 continues to grow above the average size of L1210 cells at the mitotic entry (gray dashed line). **b,c**, Buoyant mass (black), SNACS (red) and FUCCI (green, mAG-hGem) of a control L1210 cell (**b**) and a L1210 cell treated with 10  $\mu$ M ethylisopropylamiloride (EIPA, an inhibitor of Na<sup>+</sup>/H<sup>+</sup> antiporters) (**c**). Fluorescence detection limit of our system is shown by a green band in the bottom. An abrupt decrease in FUCCI (degradation of Geminin) marks the metaphase-anaphase transition. Vertical lines separate the cell cycle positions marked by color bars as shown in Fig. 3c. P: prophase, M: metaphase, A: anaphase, T: telophase.



Supplementary Figure 11

**The rate of swelling does not affect SNACS change.**

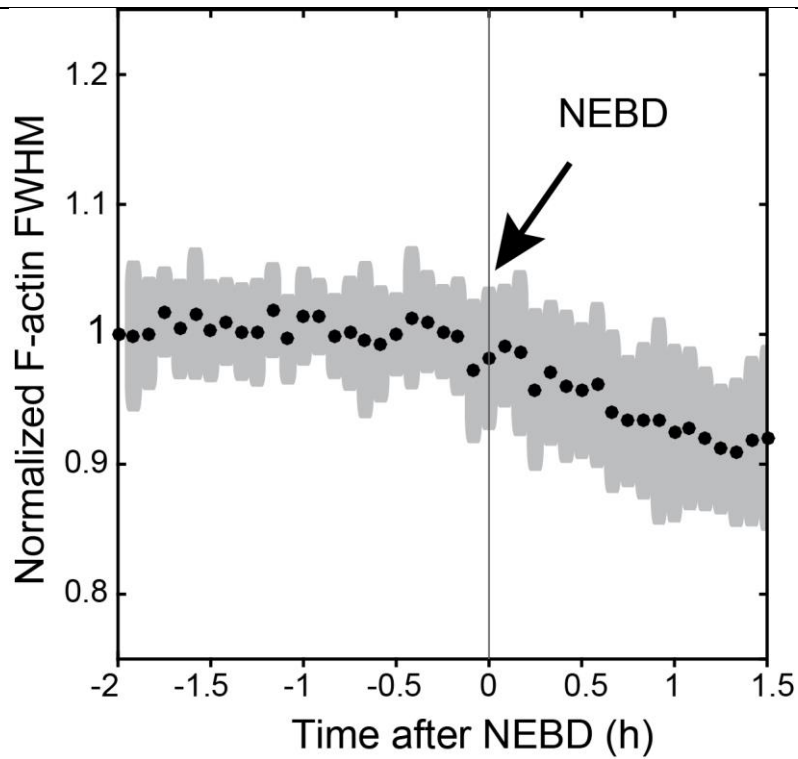
Two independent experiments showing SNACS change relative to controls (red, n=637 and 566 cells for replicate #1 and #2, respectively) upon hypotonic shocks that are slow (dark blue,  $-\Delta 50$  mOsm over 20 minutes, n=558 and 544 cells for replicate #1 and #2, respectively) or fast (light blue,  $-\Delta 50$  mOsm instantaneous, n=507, 569 cells for replicate #1 and #2, respectively). Boxes: interquartile range, squares: mean, whiskers: 5-95%; \*\*\*\* $P < 0.0001$ , n.s., not significant.  $P$  (control vs Hypotonic, slow) =  $2.82 \times 10^{-11}$  and  $9.8 \times 10^{-18}$ ,  $P$  (control vs Hypotonic, fast) =  $6.63 \times 10^{-14}$  and  $5.1 \times 10^{-15}$ ,  $P$  (Hypotonic, slow vs Hypotonic, fast) = 0.32 and 0.36 for replicate #1 and #2, respectively. P values are obtained by one-way ANOVA, Fisher's LSD.



**Supplementary Figure 12**

**Illustration of the image analysis.**

**a-h**, Successive steps of image analysis to obtain full width at half maximum (FWHM) of F-actin cortex in early mitosis: Deconvolved image of the LifeAct signal from a L1210 FUCCI cells expressing LifeAct-RFP F-actin probe (**a**). The image after applying median filter (**b**). Binary converted image (**c**). Automatic detection of cell boundaries (red circle) (**d**). 100 radial paths (yellow lines) on which the LifeAct signal was quantified (**e**). Overlay of all radial path signals (yellow) as a function of distance from the cell center (**f**). The median of the radial paths (black line) was used to determine baseline within the cell, maximum signal at the actin cortex and, consequently, the full width at half maximum (FWHM). **g,h**, Nuclear envelope breakdown (NEBD) was used for aligning different cells to the same point in the cell cycle. NEBD was detected by the abrupt spread of the green Geminin fluorescence of the FUCCI from a restricted nuclear localization (**g**) to the whole cytoplasm (**h**). **i-l**, Successive steps of image analysis to detect equatorial and polar regions of the F-actin cortex in late mitosis. Steps in order (top to bottom) and from different time points (left to right): Deconvolved image of a L1210 FUCCI cell expressing LifeAct-RFP F-actin probe (**i**). Detection of one or two cells in the image (red circles) (**j**). Assigning of the polar regions (white areas) (**k**). Assigning of the equatorial regions (white areas) (**l**). See Methods for additional details.

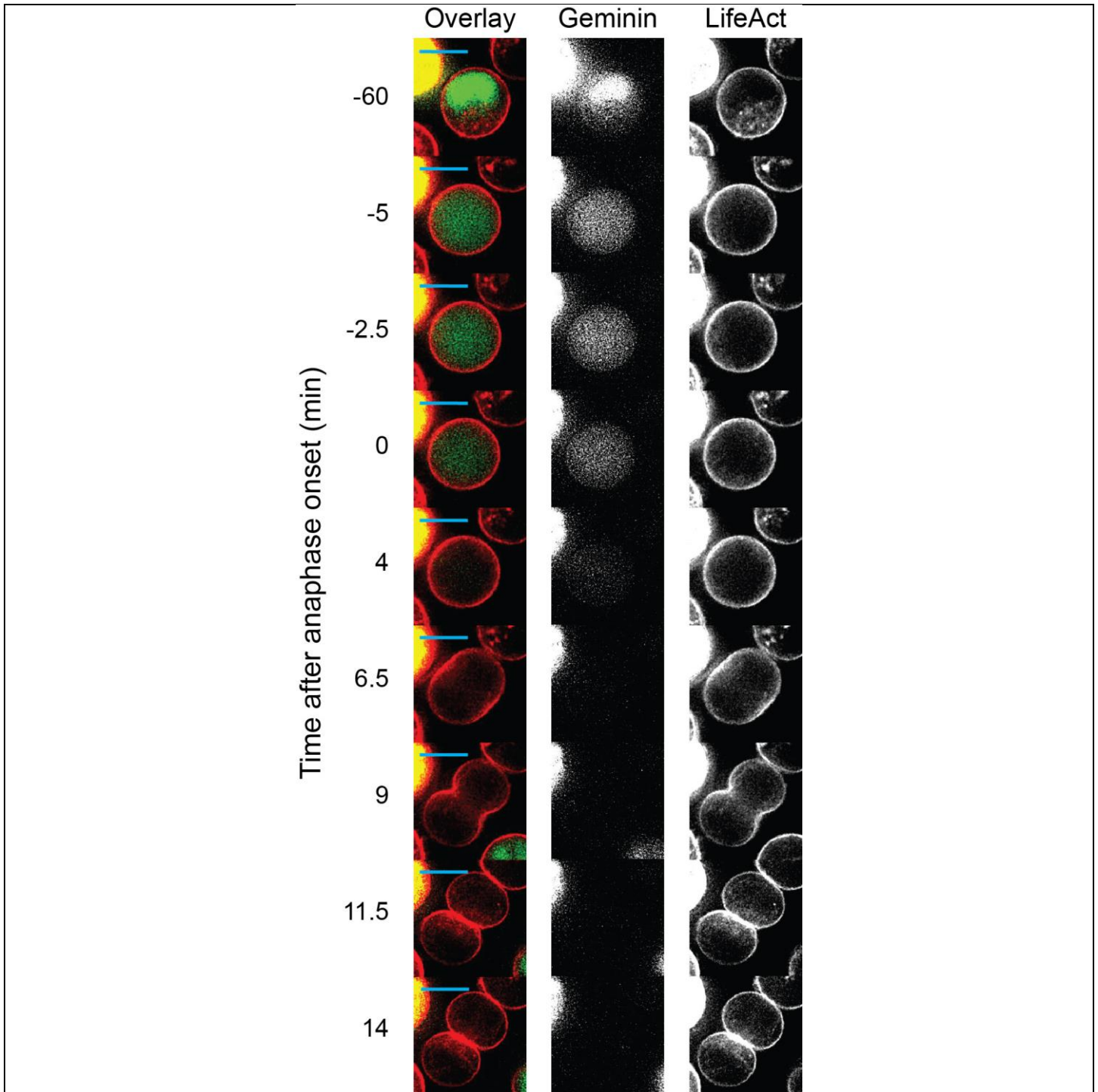


**Supplementary Figure 13**

**F-actin cortical thickness decreases in early mitosis.**

Mean full width at half maximum (FWHM, proxy of cortical thickness, black dots) and  $\pm$  s.d. (gray bars) of cortical LifeAct signal from L1210 FUCCI cells expressing LifeAct-RFP F-actin probe in early mitosis (n = 29 cells). All FWHM signal was normalized to the time point at t = -2 h. Time zero marks nuclear envelope breakdown (NEBD).

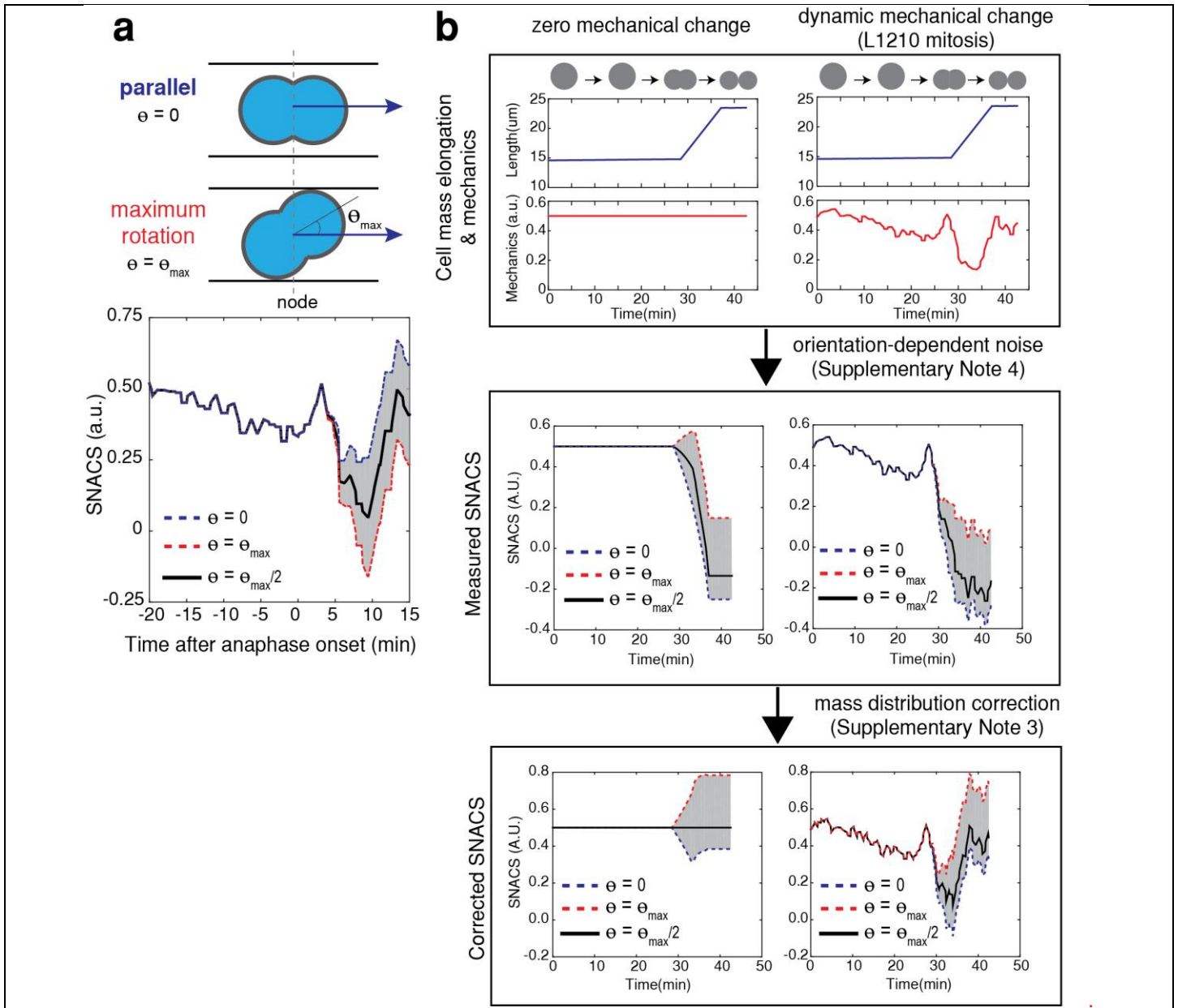




**Supplementary Figure 14**

**Fluorescence images of F-actin and FUCCI in late mitosis.**

Left column (Overlay), overlay of LifeAct (F-actin probe, red channel) and FUCCI (mAG-hGem, green channel) as a function of time after anaphase onset ( $n = 7$  cells undergoing mitosis). Scale bars, 10  $\mu\text{m}$ . Middle column (Geminin), fluorescence from the green channel only. Right column (LifeAct), fluorescence from the red channel only.



Supplementary Figure 15

**Orientation-dependent noise and mass distribution correction during late mitosis.**

**a**, Top, schematic showing the two extreme orientations of a cell during late mitosis: cells flowing parallel to the channel ( $\theta = 0$ ) and maximally rotated ( $\theta = \theta_{max}$ ). Note that dimension of the channel walls (black lines) and elongation length of a cell at a given time point determines maximal rotation angle ( $\theta_{max}$ ). Bottom, SNACS is corrected assuming three different orientations relative to the channel when cell is at the node:  $\theta = 0$  (blue dash),  $\theta = \theta_{max}$  (red dash) and  $\theta = \theta_{max}/2$  (black solid). Gray area marks the orientation-dependent noise. See Supplementary Fig. 9 for raw SNACS. **b**, Effect of uncertainty in cell orientation on measured SNACS and corrected SNACS for two hypothetical cells both elongating as L1210 cells in mitosis (top panel, blue), but with different mechanical changes (top panel, red): zero change (left) and dynamic mechanical change similar to L1210 cells in mitosis (right). Two extreme orientations illustrated in **a** marks the boundary (blue and red dash) of orientation-dependent noise (gray area) in measured SNACS (middle panel). Corrected SNACS signals assuming an intermediate orientation ( $\theta = \theta_{max}/2$ ) during the entire time course are shown in the bottom panel. Representation of SNACS traces corresponding to each orientation are the same as in **a**. See Supplementary Note 4.3 for additional details.

